Static fluctuations of a thick one-dimensional interface in the $1 + 1$ directed polymer formulation: Numerical study

Elisabeth Agoritsas,[1,*] Vivien Lecomte,[1,2] and Thierry Giamarchi[1]

[1]*DPMC-MaNEP, University of Geneva, 24 Quai Ernest-Ansermet, 1211 Geneva 4, Switzerland*

[2]*Laboratoire Probabilités et Modèles Aléatoires (CNRS UMR 7599), Universités Paris VI et Paris VII,*

Bâtiment Sophie Germain, Avenue de France, 75013 Paris, France

We study numerically the geometrical and free-energy fluctuations of a static one-dimensional (1D) interface with a short-range elasticity, submitted to a quenched random-bond Gaussian disorder of *finite* correlation length $\xi > 0$ and at finite temperature T. Using the exact mapping from the static 1D interface to the $1 + 1$ directed polymer (DP) growing in a continuous space, we focus our analysis on the disorder free energy of the DP end point, a quantity which is strictly zero in the absence of disorder and whose sample-to-sample fluctuations at a fixed growing time t inherit the statistical translation invariance of the microscopic disorder explored by the DP. Constructing a new numerical scheme for the integration of the Kardar-Parisi-Zhang evolution equation obeyed by the free energy, we address numerically the time and temperature dependence of the disorder free-energy fluctuations at fixed finite ξ. We examine, on one hand, the amplitude $\widetilde{D}_t$ and effective correlation length $\tilde{\xi}_t$ of the free-energy fluctuations and, on the other hand, the imprint of the specific microscopic disorder correlator on the large-time shape of the free-energy two-point correlator. We observe numerically the crossover to a low-temperature regime below a finite characteristic temperature $T_c(\xi)$, as previously predicted by Gaussian variational method computations and scaling arguments and extensively investigated analytically in [Phys. Rev. E **87**, 042406 (2013)]. Finally, we address numerically the time and temperature dependence of the roughness $B(t)$, which quantifies the DP end point transverse fluctuations, and we show how the amplitude $\widetilde{D}_\infty(T,\xi)$ controls the different regimes experienced by $B(t)$—in agreement with the analytical predictions of a DP toy model approach.

I. INTRODUCTION

Consider a material constituted of a large number of elements which interact locally. Long-range correlations are known to arise in such systems close to the critical point of a second-order phase transition, leading generically to scale-invariant structures [1]. Another situation where the collective behavior of the system constituents also induces correlations at large length scales is given by the boundaries of coexisting different phases, which define interfaces. Examples of such systems range from growth interfaces [2,3] of crystals adsorbing dissolved molecules to domain walls (DWs) in ferromagnetic [4–6] or ferroelectric [7–9] thin films, interfaces in turbulent liquid crystals [10–12], fronts of combustion in burning paper [13,14], fractures in paper [15], or contact lines in wetting experiments [16,17]. Such experimental interfaces exhibit a self-similarity at large length scales, which is characterized by a "roughness exponent," ζ [1,3]. They can be studied in the generic framework of *disordered elastic systems* (DES) [18], in which a one-dimensional (1D) interface is described as an elastic string fluctuating in a two-dimensional disordered energy potential. The elasticity of the string tends to minimize its distortions while the disorder (accounting for inhomogeneities in the underlying medium), concurrent with the thermal noise, induces ample geometrical fluctuations and yields metastability and glassy properties [19]. Once the dimensionality, the elasticity, and the type of disorder are given, the corresponding Hamiltonian of the DES modeling

fully determines the universality class and the value of the roughness exponent ζ. However, an additional physical ingredient that must be included in a realistic DES modeling of experimental systems is the existence of a finite microscopic width of the interface or, equivalently, a finite disorder correlation length $\xi > 0$. The subtle interplay between this finite width and thermal fluctuations at finite temperature T raises challenging issues from an analytical point of view, with relevant implications for experimental systems [18].

For 1D interfaces, two universality classes of geometrical fluctuations have actually emerged from a theoretical point of view: the Edwards-Wilkinson (EW) class [20] and the Kardar-Parisi-Zhang (KPZ) class [21], with, respectively, $\zeta_{EW} = 1/2$ and $\zeta_{KPZ} = 2/3$. A fruitful approach to study the fluctuations of a static 1D interface consists in adopting the $1 + 1$ directed polymer (DP) description, as illustrated in Fig. 1: In a fixed disorder potential $V(t,y)$, a segment of the interface of length t_1 is described as the path $y(t)$ of a DP starting from a fixed origin and growing along a time direction t up to a final time t_1. With the equivalence between the interface length scale and the DP growing time, a central quantity to study is the free energy $F_V(t,y)$ associated to the trajectories passing through y at time t. Indeed, a complete characterization of the fluctuations of the 1D interface then amounts to the determination of the whole statistical distribution of this free energy as a function of time. This distribution encodes in particular the geometrical fluctuations of the interface as a function of the length scale, which are directly measurable experimentally and whose variance defines the *roughness* function $B(t)$ (see Fig. 1), following asymptotically the power law $B(t) \sim t^{2\zeta}$.
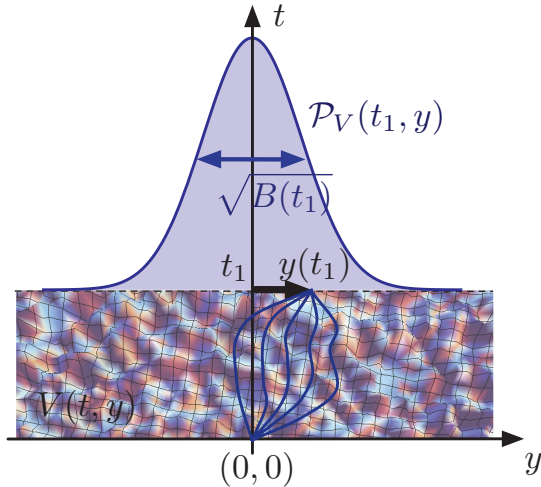
*elisabeth.agoritsas@unige.ch

FIG. 1. (Color online) The paths represent different realizations of a static 1D interface of length t_1 in the $1+1$ DP representation: One polymer extremity is attached at a fixed origin $(0,0)$ while its end point at time t_1 is fluctuating. In a given disorder realization $V(t,y)$, the distribution of the end point $y_1 = y(t_1)$ is denoted by $\mathcal{P}_V(t_1,y_1)$ and its mean variance at time t_1 defines the DP "roughness" $B(t_1)$. The DP description of the interface as growing along a "time" direction allows us to use tools of stochastic processes and amounts, in the language of the 1D interface, to study the effective statistics of the DP end point at a fixed length scale t_1, having integrated the fluctuations at shorter length scales.

We focus on the case of a 1D interface with a short-range elasticity and a quenched random-bond Gaussian disorder, which yields a generic continuous model belonging to the KPZ universality class [3,21–23]. A large variety of problems actually belong to this class, such as random matrix models [22,24], the noisy Burgers equation in hydrodynamics [25,26], population dynamics in random environments [27], one-dimensional growth phenomena [2], last-passage percolation [28], dynamics of cold atoms [29], or vicious walkers [30–32]. There has been a recent increase of interest in this class of problems in both physics [30,33,34] and mathematics [35,36]: It indeed has been shown in those references that, for an *uncorrelated disorder* ($\xi = 0$), the complete scaling of the free-energy fluctuations at all times has been elucidated, in the sense that the free energy not only presents the universal roughness exponent $\zeta_{KPZ} = 2/3$ [24,37–39] but also, once properly rescaled, follows a universal distribution at asymptotically large time. The case of a disordered potential *correlated at short length scales* ($\xi > 0$), however, challenges possible universality features and proves more difficult to tackle, thus, fewer results are available. Such correlations are, nevertheless, particularly relevant to understand experimental results: The $\xi = 0$ limit is indeed only an ideal limit since disordered materials always present correlations at a short scale $\xi > 0$; besides, one can show that thick interfaces (e.g., ferromagnetic DWs) are equivalent to pointlike interfaces with finite ξ, in the DES description [40]. In Refs. [18,40] we have shown, with scaling arguments and Gaussian variational method (GVM) computations, that a characteristic temperature $T_c(\xi)$ separates two regimes for the roughness. At high temperatures well above T_c, the microscopic correlation length

ξ plays no role and the disorder can as well be assumed to be uncorrelated, whereas at low temperatures below T_c it plays a role *at all length scales*, even macroscopically. The central quantity that controls this temperature crossover turns out to be the asymptotic free-energy amplitude $\widetilde{D}_\infty$, which also rules the roughness amplitude and characteristic crossover length scales. Actually, the existence of such a temperature-dependent parameter was already hinted at numerically in Ref. [41], for both a continuous and a discrete DP, as a fitting parameter in order to test a scaling relation between the free-energy global scaling properties and the DP geometrical fluctuations. In Ref. [42] we have investigated analytically the time and temperature dependence of the free-energy and geometrical fluctuations at finite ξ, providing a proper justification to a previous DP toy model for the free-energy fluctuations and, thus, of its corresponding GVM roughness predictions [40]; we have in particular obtained an analytical prediction for the full temperature-induced crossover of $\widetilde{D}_\infty(T,\xi)$. However, a numerical counterpart to this investigation was needed in order to complete and test these analytical results and is, thus, the object of the present study.

In this paper, we propose a novel numerical scheme to integrate the KPZ equation *with colored noise* which governs the evolution of the free energy $F_V(t,y)$, with the so-called "sharp-wedge" initial conditions. Usual procedures are either afflicted with discretization issues [28] and/or by the predominance at short times of thermal fluctuations, which obfuscate the genuine effects of disorder. The numerical evaluation that we have designed works directly in the continuum and uses a symmetry that allows us to focus on the sole disorder contribution to the free energy. It allows us to sample this "disorder free energy" $\bar{F}_V(t,y)$ on a wide range of times and temperatures at fixed ξ. We perform an extensive test of the assumptions made in the analytical approach put forward in our companion paper [42], assessing primarily the validity of our DP toy model with respect to the full free-energy fluctuations and the qualitative agreement of its GVM predictions for the roughness function. We observe in particular the predicted monotonous crossover to the low-temperature regime for the amplitude $\widetilde{D}_\infty(T,\xi)$. Our numerical approach also probes successfully the KPZ-specific nonlinearities together with hallmarks of the non-Gaussianity of the free-energy distribution. We emphasize that our proposed procedure is of general purpose, given the richness of the KPZ universality class, even if we apply it here to tackle specifically issues of the finite width of a 1D interface at finite temperature.

The plan of the paper is as follows. In Sec. II we detail the $1+1$ directed-polymer model, making the link with the static 1D interface and presenting the open questions at $\xi > 0$ that we examine. In Sec. III we discuss the specific difficulties of simulating the KPZ equation and we expose the numerical procedure that we have used in this paper before moving to the three parts of our numerical results. First, we study, in Sec. IV, the time evolution of the disorder free-energy fluctuations at fixed temperature via the two-point correlator of interest denoted $\bar{R}(t,y)$. In order to test our DP toy model, we measure its amplitude $\widetilde{D}_t$ and correlation length $\widetilde{\xi}_t$ assuming different shapes of the correlator. Second, we focus in Sec. V on the large-time saturation of this effective disorder correlator and its temperature dependence, measuring in particular the full

temperature-induced crossover of the amplitude $\widetilde{D}_\infty(T,\xi)$. Third and last, we investigate, in Sec. VI, the temperature dependence of the roughness function $B(t)$ and its effective scale-dependent exponent $\zeta(t)$. We present our conclusions in Sec. VII. Appendices gather part of the technical details and thorough numerical analyses.

II. 1 + 1 DIRECTED-POLYMER FORMULATION OF THE STATIC 1D INTERFACE

In this section, we define the continuous $1 + 1$ DP formulation of the 1D interface model that we study, together with our observables of interest at a fixed length scale or DP growing time, as first set in Fig. 1. After recalling its known analytical properties, we present the DP toy model discussed in Ref. [42] and ultimately aimed at grasping the temperature dependence of the 1D interface geometrical fluctuations.

A. Model

From the point of view of the interface, the energy associated to a segment of length (or "time") t_1 is the sum of a short-range quadratic elastic cost and of the total potential energy accumulated along the line in a fixed disorder landscape $V(t,y)$.

Let us, first, precisely define the *unnormalized* Boltzmann weight $W_V(t_1,y_1)$ of trajectories starting at the fixed origin $(0,0)$ and ending at (t_1,y_1) as follows:

$$W_V(t_1,y_1) = \int_{y(0)=0}^{y(t_1)=y_1} \mathcal{D}y(t)\, e^{-\mathcal{H}[y,V;t_1]/T}, \qquad (1)$$

where the DES energy of the line is the sum of the integrated elastic and disorder contributions,

$$\mathcal{H}[y,V;t_1] = \int_0^{t_1} dt \left[\frac{c}{2}(\partial_t y(t))^2 + V(t,y(t))\right], \qquad (2)$$

with c the elastic constant. The Boltzmann constant is conveniently set to $k_B = 1$ such that the temperature has the unit of an energy.

Importantly, the disorder potential $V(t,y)$ is assumed to have a Gaussian distribution of zero mean and of *finite transverse correlations* described by a "colored noise" fully characterized by its two-point correlator as follows:

$$\overline{V(t,y)V(t',y')} = D\,\delta(t-t')\,R_\xi(y-y'), \qquad (3)$$

where the statistical average with respect to disorder is denoted by an overline, D is the disorder strength, and ξ its typical correlation length. We study the case of a *short-range* "random-bond" disorder potential, i.e., characterized by a correlation function $R_\xi(y)$ decaying fast enough at large y (faster than any power law). The disorder strength D is defined by fixing the normalization of $R_\xi(y)$ with $\int_{\mathbb{R}} dy\, R_\xi(y) = 1$. The parameter ξ is assumed to fully control the scaling of the correlator by the relation $R_\xi(y) = \frac{1}{\xi}R_1(y/\xi)$ and to fix the characteristic temperature $T_c(\xi) = (\xi c D)^{1/3}$ [18,40].

The "partition function" $Z_V(t,y)$ of the DP trajectories is written as

$$Z_V(t,y) = \frac{W_V(t,y)}{\bar{W}_{V\equiv0}(t)}, \qquad (4)$$

where $\bar{W}_{V\equiv0}(t) = \int_{\mathbb{R}} dy\, W_{V\equiv0}(t,y)$ fixes the normalization of the path integral (1). We refer the reader to Ref. [43] or Ref. [35] for mathematical constructions in different contexts and to Ref. [42] for a time-discrete *à la* Feynman approach. The fixed origin translates into the initial condition $Z_V(0,y) = \delta(y)$ and the time evolution is given by a stochastic heat equation [38,43–45],

$$\partial_t Z_V(t,y) = \left[\frac{T}{2c}\partial_y^2 - \frac{1}{T}V(t,y)\right]Z_V(t,y), \qquad (5)$$

that can be seen as a Langevin equation with multiplicative spatiotemporal "noise," $V(t,y)$, and may be understood as a "Feynman-Kac" formula [42,46–48]. In absence of disorder, $Z_{V\equiv0}(t,y)$ is a normalized Gaussian of variance $B_{th}(t) = \frac{Tt}{c}$. Note that the normalization $\bar{W}_{V\equiv0}(t)$ in (4) is essential to obtain the stochastic heat equation (5) and is usually hidden in the definition of the path integral (1).

With the disorder-dependent normalization at fixed time t,

$$\bar{W}_V(t) \equiv \int_{-\infty}^{\infty} dy\, W_V(t,y), \qquad (6)$$

we can define the probability distribution function (PDF) of the DP end point, respectively, at fixed disorder V and after the disorder average,

$$\mathcal{P}_V(t,y) \equiv \frac{W_V(t,y)}{\bar{W}_V(t)}, \quad \mathcal{P}(t,y) = \overline{\mathcal{P}_V(t,y)}. \qquad (7)$$

We emphasize that, due to different normalizations, the probability distribution $\mathcal{P}_V(t,y)$ is *not* the same as the DP partition function $Z_V(t,y)$ (4): Only the latter evolves with the stochastic heat equation (5) but they coincide in absence of disorder: $\mathcal{P}_{V\equiv0}(t,y) = Z_{V\equiv0}(t,y)$.

The corresponding free energy, defined by $F_V(t,y) \equiv -T\log Z_V(t,y)$, obeys the KPZ equation [21,38]:

$$\partial_t F_V(t,y) = \frac{T}{2c}\partial_y^2 F_V(t,y) - \frac{1}{2c}[\partial_y F_V(t,y)]^2 + V(t,y), \quad (8)$$

whose specificities arise from the nonlinear term $\left[\partial_y F_V(t,y)\right]^2$; in the absence of this nonlinearity (8) becomes the EW equation [20]. The pure thermal contribution $F_{V\equiv0}(t,y)$ can be derived from the (diffusive) solution of the problem without disorder and reads:

$$Z_{V\equiv0}(t,y) = e^{-y^2/(2B_{th}(t))}\big/\sqrt{2\pi B_{th}(t)}, \qquad (9)$$

$$F_{V\equiv0}(t,y) = F_{th}(t,y) + \frac{T}{2}\log\frac{2\pi Tt}{c}, \qquad (10)$$

$$F_{th}(t,y) = \frac{cy^2}{2t}, \quad B_{th}(t) = \frac{Tt}{c}, \qquad (11)$$

and once removed from the total free energy, it allows us to focus on the sole disorder contribution, which presents helpful statistical properties. Indeed, the *disorder free energy* defined by

$$\bar{F}_V(t,y) \equiv F_V(t,y) - F_{V\equiv0}(t,y) \qquad (12)$$

obeys the statistical tilt symmetry (STS), which states that, *at fixed time t*, the distribution of $\bar{F}_V(t,y)$ is invariant by translation along the transverse direction y,

$$\bar{\mathcal{P}}[\bar{F}_V(t,y+Y)] = \bar{\mathcal{P}}[\bar{F}_V(t,y)]. \qquad (13)$$

We refer the reader to Refs. [19,35,49–51] for previous discussions of the STS and to Ref. [42] for a derivation at finite ξ. Moreover, this definition of the disorder free energy implies that $\bar{F}_V(t,y)$ evolves with a "tilted" KPZ equation at $t > 0$ as follows:

$$\partial_t \bar{F}_V(t,y) = \frac{T}{2c} \partial_y^2 \bar{F}_V(t,y) - \frac{1}{2c}[\partial_y \bar{F}_V(t,y)]^2$$
$$- \frac{y}{t} \partial_y \bar{F}_V(t,y) + V(t,y). \qquad (14)$$

Note that neglecting the nonlinearity in this evolution does not yield the EW equation, since the linear tilt $\frac{y}{t}\partial_y \bar{F}_V(t,y)$ itself stems from the KPZ nonlinearity in (8). The initial condition $Z_V(0,y) = \delta(y)$, which is difficult to express for the free energy $F_V(t,y)$ (this is the "sharp-wedge" initial condition [52]), translates simply for the disorder free energy into $\bar{F}_V(0,y) \equiv 0$, since the Dirac δ function is absorbed by the thermal $Z_{V\equiv0}(0,y) = \delta(y)$.

B. Disorder free-energy fluctuations and DP toy model

We may assume that the scaling of the distribution $\bar{\mathcal{P}}[\bar{F},t]$ is in large part controlled by the translation-invariant two-point disorder correlators defined by

$$\bar{C}(t,y_2 - y_1) \equiv \overline{[\bar{F}_V(t,y_1) - \bar{F}_V(t,y_2)]^2}, \qquad (15)$$

$$\bar{R}(t,y_2 - y_1) \equiv \overline{\partial_y \bar{F}_V(t,y_1)\partial_y \bar{F}_V(t,y_2)}, \qquad (16)$$

where the functions $\bar{R}(t,y)$ and $\bar{C}(t,y)$ are even functions of y and are related through $\partial_y^2 \bar{C}(t,y) = 2\bar{R}(t,y)$ [42]. Note that although the study of $\bar{C}(t,y)$ is a natural choice as it characterizes the second moment of $\bar{F}_V$, we have argued in Ref. [42] that the study of $\bar{R}(t,y)$ yields a clearer physical picture. In particular, its value at $y = 0$ characterizes the fluctuations of the KPZ nonlinearity in the evolution equation (14) as $\bar{R}(t,0) = \overline{[\partial_y \bar{F}_V(t,y)]^2}$.

For an *uncorrelated disorder*, i.e., for $R_\xi(y) = \delta(y)$ in (3) or, equivalently, $\xi = 0$, it has been shown that the features shared in the KPZ universality class consist not only of the value of roughness scaling exponent $\zeta_{KPZ} = 2/3$ but also of the asymptotic *distribution* of the free energy. More precisely, the disorder free energy $\bar{F}_V(t,y)$ scales in distribution at large times according to

$$\bar{F}_V(t,y) \overset{d}{=} \left(\frac{\widetilde{D}_\infty^2}{c}t\right)^{\frac{1}{3}} \mathcal{A}_2(y/\sqrt{B_{RM}(t)}) \quad \text{as } t \to \infty, \qquad (17)$$

$$B_{RM}(t) \sim \left(\frac{\widetilde{D}_\infty}{c^2}\right)^{\frac{2}{3}} t^{\frac{4}{3}}, \quad \widetilde{D}_\infty = \frac{cD}{T}, \qquad (18)$$

where $\mathcal{A}_2(\bar{y})$ is the so-called Airy$_2$ process [53], independently of the system DES parameters $\{c,D,T\}$, and $B_{RM}(t)$ is the roughness in the asymptotic "random manifold" (RM) regime. As stated in the introduction, the parameter $\widetilde{D}_\infty$ is central in our analysis, being common to the free-energy scaling in distribution (17) and to the scaling of the large-time roughness amplitude (18). The scaling relations (17) and (18) express the fact that in addition to the universality of the exponents, the amplitudes and the free-energy distribution are also universal in the $\xi = 0$ KPZ class.

At $\xi = 0$ the mere relation $\widetilde{D}_\infty = \frac{cD}{T}$ holds exactly. However, the crucial point for the short-range correlated case $\xi > 0$ is that it must be generalized to

$$\widetilde{D}_\infty(T,\xi) \equiv f(T,\xi)\frac{cD}{T}, \qquad (19)$$

where $f(T,\xi)$ is an interpolating parameter such that the correct uncorrelated limit $\widetilde{D}_\infty(T,0) = \frac{cD}{T}$ is recovered, with $f(T,0) \equiv 1$. In Ref. [42] we have predicted a monotonous behavior of $\widetilde{D}_\infty$ as a function of temperature T, described by $f(T,\xi)$ being the solution of the equation $f^\gamma \propto [\frac{T}{T_c(\xi)}]^\gamma(1 - f)$. Note that the exponent γ takes different values $\gamma > 0$ depending on the approximation scheme considered but always predicts a saturation of the amplitude at zero temperature: $\widetilde{D}_\infty(0,\xi) \sim \frac{cD}{T_c}$.

In Ref. [41], we have shown numerically with other coauthors that the scaling relation (17) can be extended to the correlated case $\xi > 0$ with a modified Airy$_2$ process (still to be characterized) and by replacing the asymptotic $B_{RM}(t)$ in (18) by the actual roughness $B(t)$. However, the characterization of this modified Airy$_2$ process will require the understanding of a scaling relation valid on the *full transverse range y*, and this generalized scaling relation has actually been tested by the numerical collapse of the full correlator $\bar{C}(t,y)$ (15) at different times and temperatures. In addition, in the companion paper [42], we have centered our analytical study on the *local* scaling properties of the correlator $\bar{R}(t,y)$ (16), which actually characterizes the fluctuations of the KPZ nonlinearity in (14). We have showed that this *a priori* perplexing observable captures in fact the entire crossover from the low- to the high-temperature regime through its *small-y* behavior. In a DP toy model approach, we have thus advocated that, at least for $|y| \lesssim \xi$ and sufficiently large times, the correlator $\bar{R}(t,y)$ takes the form

$$\bar{R}(t,y) \approx \widetilde{D}_t \mathcal{R}_{\tilde{\xi}_t}(y), \quad \int_{\mathbb{R}} dy\, \mathcal{R}_{\tilde{\xi}_t}(y) \equiv 1, \qquad (20)$$

where the normalized function $\mathcal{R}_{\tilde{\xi}_t}(y)$ is assumed to take a stabilized form closely related to the disorder correlator $R_\xi(y)$ defined by (3), in the sense that these correlators share the same scaling in $\tilde{\xi}_t \propto \xi$. All possible time dependence is then hidden in two effective parameters, $\widetilde{D}_t$ and $\tilde{\xi}_t$, and at asymptotically large times a steady state is reached with $\bar{R}(\infty,y) \equiv \widetilde{D}_\infty \mathcal{R}_{\tilde{\xi}_\infty}(y)$ and in particular $\bar{R}(\infty,0) \sim \widetilde{D}_\infty/\tilde{\xi}_\infty$. This behavior suggests the definition of a *saturation time* t_{sat} above which

$$\bar{R}(t,|y| \lesssim \xi) \approx \widetilde{D}_\infty \mathcal{R}_{\tilde{\xi}_\infty}(y) \equiv \bar{R}_{sat}(y). \qquad (21)$$

The crossover of $\widetilde{D}_\infty(T,\xi)$ announced in (19) stems from the subtle interplay of the KPZ nonlinearity feedback with the disorder $V(t,y)$ for short times $t \lesssim t_{sat}$.

The ansatz (20) has been inspired by the infinite-time limit of the free-energy fluctuations, respectively, for the uncorrelated case [38] and for the linearized version of the tilted KPZ equation (14) presented in Ref. [42] (whose solution is denoted thereafter by a subscript "lin"). In both cases the fluctuations are Gaussian and, thus, fully characterized by their two-point correlators,

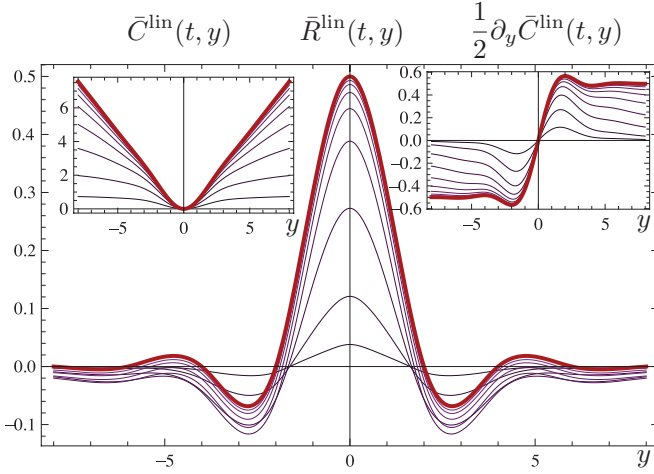$$\bar{R}(\infty,y) \overset{(\xi=0)}{=} \frac{cD}{T}R_{\xi=0}(y), \quad R_{\xi=0}(y) = \delta(y), \qquad (22)$$

FIG. 2. (Color online) The finite-time correlator $\bar{R}^{\text{lin}}(t,y)$ (thin purple lines) for the CubicS disorder correlator $R_\xi(y) = R_\xi^{\text{CubicS}}(y)$ defined in (A2) and (A3) and plotted as a function of y for different times and compared to its infinite-time limit $R_\xi(y)$ (thick red line). The central peak develops with increasing times from the flat initial condition $\bar{R}(0,y) \equiv 0$. Parameters are $\xi = 2$, $c = 1$, $D = 1$, and $T = 1$. Left inset: Same behavior for $\bar{C}^{\text{lin}}(t,y)$. Right inset: Same behavior for $\frac{1}{2}\bar{C}^{\text{lin}}(t,y) = \int_0^y dy'\, \bar{R}^{\text{lin}}(t,y')$.

$$\bar{R}^{\text{lin}}(\infty,y) = \widetilde{D}_\infty\, R_\xi(y), \quad \widetilde{D}_\infty = \frac{cD}{T}. \tag{23}$$

As discussed in Ref. [42], the linearized case—which is *not* equivalent to a standard EW evolution for $\partial_t F_V(t,y)$ [20]—has been solved exactly at all times, predicting Gaussian fluctuations and yielding the following decomposition:

$$\bar{R}^{\text{lin}}(t,y) = \frac{cD}{T}[R_\xi(y) - b^{\text{lin}}(t,y)], \tag{24}$$

with $\lim_{t \to \infty} b^{\text{lin}}(t,y) = 0$. This behavior is depicted in Fig. 2 for the specific disorder correlator that will be used in our numerical simulations $R_\xi^{\text{CubicS}}(y)$, defined in (A2) and (A3). Note that the disorder free-energy fluctuations are non-Gaussian in the full nonlinearized case, except in the very specific limit of infinite time and uncorrelated disorder $\xi = 0$, requiring, thus, the complete set of n-point correlator to characterize them. Nevertheless, the solution (24) suggests a similar decomposition for the exact two-point correlator $\bar{R}(t,y)$, separating its asymptotic amplitude $\widetilde{D}_\infty$ and shape $\mathcal{R}_\xi(y)$ from a finite-time contribution $b(t,y)$ under the exact constraint that $\int_{\mathbb{R}} dy\, \bar{R}(t,y) = 0$ at $t < \infty$ [42],

$$\bar{R}(t,y) = \widetilde{D}_\infty\, [\mathcal{R}_\xi(y) - b(t,y)], \tag{25}$$

$$\int_{\mathbb{R}} dy\, \mathcal{R}_\xi(y) \equiv 1 \implies \int_{\mathbb{R}} dy\, b(t,y) = 1 \quad \forall t, \tag{26}$$

$$\lim_{t \to \infty} b(t,y) = 0. \tag{27}$$

The scaling of $b(t,y)$ corresponds to the "wings" of the alternative correlator $\bar{C}(t,y)$ (15), which rescales with the roughness $B(t)$ as studied extensively in Ref. [41].

It is striking that the $\xi = 0$ result (22) holds in the same form in the linearized and nonlinearized evolutions of the disorder free energy, with the imprint of the microscopic disorder correlator at large times such that $\mathcal{R}_{\xi_\infty}(y) = R_{\xi=0}(y)$.

This implies that any modification of both the amplitude $\widetilde{D}_\infty$ and the shape $\mathcal{R}(y)$, along with the non-Gaussianity of the free-energy fluctuations, must stem from the KPZ nonlinearity in (14).

From an analytical point of view, the validity of the ansatz (20) must still be asserted. The exact contribution $b(t,y)$ and the asymptotic temperature-dependent shape $\mathcal{R}(y)$ remain unknown for the time being, and, hence, the present numerical study is a first step in the characterization of the modified Airy$_2$ process at $\xi > 0$ in (17). In this paper we examine specifically the validity of the DP toy model centered on (20) by measuring numerically the time evolution of the correlator $\bar{R}(t,y)$ and characterizing its small-y features with respect to the microscopic disorder correlator $R_\xi(y)$ (see Secs. IV and V). We discuss, moreover, the existence of the saturation time t_{sat} and the consequent characterization of $\bar{R}_{\text{sat}}(y)$ with $\{\widetilde{D}_\infty, \tilde{\xi}_\infty, \mathcal{R}\}$ following the definition (21).

C. Geometrical fluctuations and roughness

The geometrical fluctuations of the polymer end point at time t, or, equivalently, of the interface at a given length scale t, are of high relevance because they are directly accessible, both numerically and experimentally. Their PDF $\mathcal{P}(t,y)$ (7) can be characterized mainly by its variance, namely the roughness function $B(t)$, and by an effective roughness exponent $\zeta(t)$, respectively defined as

$$B(t) \equiv \overline{\langle y(t)^2 \rangle} = \int_{\mathbb{R}} dy\, y^2\, \mathcal{P}(t,y), \tag{28}$$

$$\zeta(t) \equiv \frac{1}{2}\frac{\partial \log B(t)}{\partial \log t}, \tag{29}$$

where the brackets $\langle \mathcal{O} \rangle$ denote the statistical average over thermal fluctuations for an observable $\mathcal{O}$. It is known that the roughness is characterized at small t by the EW exponent $\zeta_{\text{EW}} = 1/2$ and at asymptotically large t by the KPZ exponent $\zeta_{\text{RM}} = \zeta_{\text{KPZ}} = 2/3$ in the RM regime. Beyond these exponents, the amplitudes of the corresponding power laws are in fact of interest and their scalings read

$$B(t) = \begin{cases} B_{\text{th}}(t) = \frac{T}{c}t^{2\zeta_{\text{EW}}} & \text{for } t \to 0 \\ B_{\text{RM}}(t) \sim \left(\frac{\widetilde{D}_\infty}{c^2}\right)^{\frac{2}{3}} t^{2\zeta_{\text{KPZ}}} & \text{for } t \to \infty \end{cases}, \tag{30}$$

as already defined respectively in (11) and (18). The large-time result is known to hold exactly with $\widetilde{D}_\infty = \frac{cD}{T}$ for an uncorrelated disorder ($\xi = 0$). In a GVM approach based on our DP toy model [18,40,41], we have, moreover, showed that it should also hold for a correlated disorder ($\xi > 0$) for all temperatures, with $\widetilde{D}_\infty(T,\xi)$ characterizing the amplitude of the free-energy fluctuations, as stated in (17)–(19).

An important crossover length scale is the Larkin length L_c [54] which marks the beginning of the RM regime and is closely related to $\widetilde{D}_\infty(T,\xi)$ [42]. Note that by consistency the Larkin length should be larger than the saturation time for the free-energy fluctuations [defined by (21)], so we expect $t_{\text{sat}} \lesssim L_c$.

One aim of this paper is to provide a numerical check of these GVM predictions (see Sec. VI), especially in order to probe intermediate regimes and length scales between the two opposite asymptotic regimes of the roughness (30). This

numerical study of the roughness at $\xi > 0$ provides, moreover, an indirect test of the validity of our DP toy model, on which these GVM predictions are based.

III. NUMERICAL RECIPE

In this section we discuss the possible numerical approaches to these problems and we expose our numerical procedure. All the numerical parameters are gathered in Appendix B.

In the next three sections, we present the different numerical results obtained, which are as follows: in Sec. IV, the time evolution of the correlator at fixed temperature $\bar{R}(t,y)$ (16) and its parameters $\{\tilde{\xi}_t, \widetilde{D}_t\}$ (20); in Sec. V, the temperature dependence of the asymptotic effective correlator $\bar{R}_{\rm sat}(y)$ and $\{\widetilde{D}_\infty, \tilde{\xi}_\infty, \mathcal{R}\}$ according to (21); and, in Sec. VI, the temperature dependence of the roughness $B(t)$ (28) and its logarithmic slope $\zeta(t)$ (29). In addition, Appendix C gathers the details of a quantitative test of the DP toy model by comparing three fitting functions for $\mathcal{R}(y)$ and Appendix D presents a self-consistency check of our numerical procedure by analyzing the time and temperature dependencies of the mean value $\overline{\bar{F}_V(t,y)} = -\frac{1}{2c}\int_0^t dt' \, \bar{R}(t',0)$.

A. Possible numerical approaches

The Feynman-Kac evolution equation (14) for the disorder free energy $\partial_t \bar{F}_V(t,y)$ provides the starting point for a numerical study of the geometrical and free-energy fluctuations of the $1+1$ DP and, consequently, of the static 1D interface, directly in their continuum formulation. This approach uses an exact property of the model—the STS (13)—to focus on the effects of the disorder, dissociated from the pure thermal ones.

Among the numerical procedures previously used to tackle this problem, we can mention, first, the DP under the solid-on-solid (SOS) constraint [41,55,56], where the polymer lives on a discretized lattice; second, the semicontinuous 1D interface, discretized along its internal dimension but with each point living in a *continuous* 1D splined random potential [57]; and, third, the continuous DP that we present thereafter. Those approaches are, of course, complementary, especially for the investigation of the large versus small length scales and high-versus low-temperature properties, if a suitable translation from the specific numerical parameters to the physical ones $\{c, D, T, \xi\}$ is provided [41,45]. The SOS model numerical approach consists in solving the discrete equivalent of the stochastic heat equation (5) onto a partition function defined on a lattice. This approach, however, proves difficult to control numerically in the low-temperature regime, since the DP end point is exponentially concentrated in favorable regions of the potential. An alternative approach thus consists in focusing on a discrete analog of the KPZ equation (8). In fact, the discretization of the nonlinear term proves to be a highly nontrivial problem even without disorder, as Kruskal and Zabusky [58] realized a long time ago in the related problem of simulating soliton solutions of the Korteweg-de Vries equation. A well-behaved lattice discretization which leads to the correct continuum limit is exposed in Ref. [28]; we refer the reader to Ref. [59] for a detailed discussion.

Our procedure is actually based on the continuous analog of the transfer-matrix method of a DP on a lattice with the SOS constraint in the sense that it is performed after integration over thermal fluctuations since it follows the evolution of the partition function $Z_V(t,y)$ with the length scale [namely the Feynman-Kac equation (14)] for many individual disorder configurations. The continuous-limit formulation has two advantages: First, the discretization issue in numerics is pushed back to a problem of numerical integration of partial differential equations, so even "small" length scales can be studied without discretization artifacts, and, second, in the continuous limit the numerical parameters are directly the physical ones of the analytical model. We refer the reader to Ref. [60] for mathematical results on the convergence of discretization schemes of the KPZ equation to the solution of the continuous equation in the situation where the disorder is spatially correlated.

B. Detailed procedure

Computing $\bar{F}_V(t,y)$ for individual disorder configurations $V(t,y)$ up to a maximal time t_m, we can measure directly the geometrical and free-energy fluctuations stemming at thermodynamic equilibrium from thermal fluctuations exploring a given random potential. Then, averaging these fluctuations over many disorder configurations, we have access to the quantities of interest defined in Sec. II.

1. Finite box and microscopic discretized grid

The Feynman-Kac evolution equation (14) is defined in a continuous limit with $t > 0$ and $y \in \mathbb{R}$. In numerics we work necessarily on a microscopic discretized grid in both (t,y) variables and in a finite box $(t,y) \in [0,t_m] \times [-y_m, y_m]$ without periodic boundary conditions. However, in experimental realizations of 1D interfaces we also have some microscopic cutoff in length scales, ultimately the crystal parameter, and a macroscopic cutoff due to scarcer statistics at larger length scales.

2. Generation of an individual disorder configuration

In order to generate individual disorder configurations for a given set of DES parameters, we first define a two-dimensional grid of spacing $\{\xi_t^{\rm grid}, \xi_y^{\rm grid}\} = \{t_m/L_t, y_m/L_y\}$ (cf. Fig. 3). On each point of the grid we pick a set of random numbers according to a normal distribution of variance $D^{\rm grid}$ (the strength of disorder) and the smooth random potential $V(t,y)$ is obtained by interpolating between the grid points with a 2D cubic spline as illustrated in Fig. 10 (top). As detailed in Appendix A, its corresponding two-point correlator at fixed time is given by the translation invariant:

$$\overline{V(t,y)V(t,0)} = D^{\rm eff} \, R_{\xi_y}^{\rm CubicS}(y), \tag{31}$$

$$D^{\rm eff} = D \, R_{\xi_t}^{\rm CubicS}(0) = D^{\rm grid}\xi_y^{\rm grid}, \tag{32}$$

with the function $R_\xi^{\rm CubicS}$ made explicit in (A2) and (A3). The values of those parameters are fixed for all our numerical computations to

$$\xi_t^{\rm grid} = 1, \quad \xi_y^{\rm grid} = 2, \quad D^{\rm grid} = 4 \;\Rightarrow\; D = D^{\rm eff} = 8. \tag{33}$$
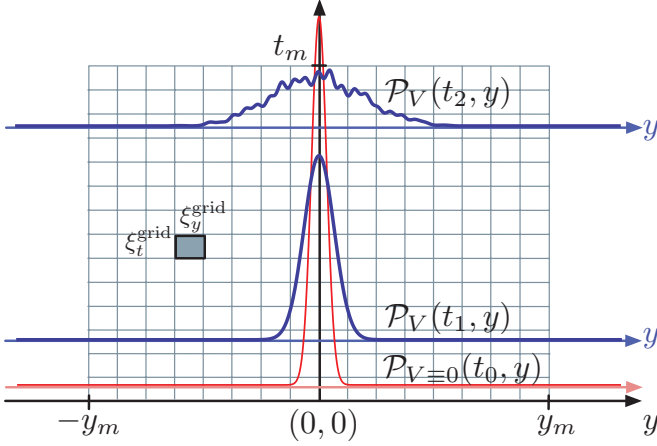
FIG. 3. (Color online) Illustration of the numerical procedure for the $1+1$ continuous DP in the finite box $[0,t_m] \times [-y_m,y_m]$ with the initial condition at $t_0 = 0.1$ taken as purely thermal $\mathcal{P}(t_0,y) = Z_{V\equiv0}(t_0,y)$ (9) (red curve). There are three levels of discretization grids by decreasing scale: the grid for the random potential $\xi_t^{\text{grid}} = 1$ and $\xi_y^{\text{grid}} = 2$ (the gray box on the left side), the linear grids for the recording of data $\Delta t^{\text{lin}} = t_m/80$ and $\Delta y^{\text{lin}} = 2y_m/100$, and the logarithmic grid $t_j^{\text{log}} = t_0\,(t_m/t_0)^{j/80}$ with $j = 0 \cdots 80$. The microscopic grid for the numerical integration is adapted in both the (t,y) directions by use of MATHEMATICA. At a given configuration of disorder $V(t,y)$ as illustrated in Fig. 10, the PDF $\mathcal{P}_V(t,y)$ is computed at increasing time following (14), with the boundary condition $\partial_y \bar{F}_V(t,\pm y_m) = 0$ and the *ad hoc* normalization (34), as illustrated at $t_0 < t_1 < t_2$ (blue curves). See Fig. 1 for the interpretation in terms of DP trajectories.

Note that the physical parameter used in analytical arguments is D (3) and not D^{eff}, but they coincide with this particular choice of ξ_t^{grid}.

3. Numerical integration at fixed disorder

We have chosen to follow the evolution of the disorder free energy $\bar{F}_V(t,y)$ (14) because among its counterparts (i) $\partial_y F_V(t,y)$ is too noisy, (ii) $F_V(t,y)$ includes $F_{\text{th}}(t,y) = \frac{cy^2}{2t}$ (11) that hides the disorder-induced fluctuations of $\bar{F}_V(t,y)$ except at large times, and (iii) the exponential in $W_V(t,y) \propto e^{-F_V(t,y)/T}$ reduces the numerical resolution. Moreover, by subtracting the exact $F_{\text{th}}(t,y)$ for $y \in \mathbb{R}$ directly in the evolution equation, we get rid of the finite-box artifacts that would have arisen already in the absence of disorder due to the pure elastic contribution. The numerical integration of the differential equation (14) was performed using a numerical algorithm included in MATHEMATICA [61], which adapts the numerical discretization in y at each time step in order to minimize the numerical errors. As emphasized in Ref. [62], pseudospectral spatial derivatives are more stable than finite differences for simulating the KPZ equation. We enforced this choice through the "DifferenceOrder"->"Pseudospectral" option to the NDSolve integrator. The main limitation was that the larger the maximum time t_m, the longer the computation time. Moreover, the lower the temperature, the more the numerical solution of the Feynman-Kac equation (14) is sensitive to the spatial variations of the random potential, thus dictating a smaller grid discretization in order to minimize the numerical error and increasing considerably the computation time. The number of disorder configurations that have been considered for a given set of DES parameters is, thus, a compromise between the convergence of the disorder average and a reasonable computation time (as summarized in Appendix B).

4. Initial condition

If, as discussed in Sec. II A, the disorder free energy $\bar{F}_V(0,y)$ is uniformly 0 at initial time $t = 0$, the equation evolution (14) for $\bar{F}_V(t,y)$ is, however, singular at $t = 0$. We thus slightly shift the initial condition to time $t_0 = 0.1$, assuming that this procedure is stable as $t_0 \to 0$. This choice corresponds to taking $\bar{F}_V(t_0,y) \equiv 0$, or, in terms of the partition function, $Z_V(t_0,y) \approx Z_{V\equiv0}(t_0,y)$ as defined by (9). For the uncorrelated case $\xi = 0$, this asymptotics $Z_V(t_0,y) \overset{t_0\to0}{\sim} Z_{V\equiv0}(t_0,y)$ has indeed been shown to be correct [63], and we assume that this result also holds in the less singular case, $\xi > 0$. We assume that at large times the DP has completely forgotten this initial condition, and we have checked numerically that this is the case for our particular choice for t_0. However, at short times above t_0, the DP behavior should carry some artifact for the disorder-induced quantities $\bar{F}_V$ and $\partial_y \bar{F}_V$.

5. Boundary conditions

We impose at each time that $\partial_y \bar{F}_V(t,\pm y_m) = 0$. This is equivalent to the statement that we have $W_V(t,y) \approx W_{V\equiv0}(t,y)$ for $|y| \geqslant y_m$ and, thus, the normalized DP end point probability can be approximated as $\mathcal{P}_V(t,y) \approx Z_{V\equiv0}(t,y) \approx 0$ (9). This boundary condition can be physically correct only for times such that $\sqrt{B(t)} < y_m$ or the DP "senses" inevitably the boundaries of the finite box. This choice of boundary condition implies for the normalization $\bar{W}_V(t)$ (6) that the contribution for displacement y outside the box $[-y_m,y_m]$ is exactly known analytically,

$$\frac{1}{2}\bar{W}_V^{\text{num}}(t) = \int_0^{y_m} dy\, e^{-(F_{\text{th}}(t,y)+\bar{F}_V(t,y))/T} + \text{cte}(t,y_m),$$
$$\text{cte}(t,y_m) = \int_{y_m}^{\infty} dy\, e^{-F_{\text{th}}(t,y)/T}, \quad F_{\text{th}}(t,y) = \frac{cy^2}{2t}. \tag{34}$$

These definitions yield back the normalized distribution $\mathcal{P}_V(t,y)$ as defined by (7) (cf. Fig. 3).

6. Recorded data

We have actually recorded, on a microscopic grid linear in y, the following quantities defined throughout Sec. II: on one hand, the disorder free energy $\bar{F}_V(t,y)$ and its derivative $\partial_y \bar{F}_V(t,y)$, with their mean values $\overline{\bar{F}_V(t,0)}$ and $\overline{\partial_y \bar{F}_V(t,0)}$ and their respective two-point correlators $\bar{C}(t,y)$ and $\bar{R}(t,y)$ [(16) and (15)] and, on the other hand, the PDFs $\mathcal{P}_V(t,y)$ and $\mathcal{P}(t,y)$, their first corresponding moments $\overline{\langle y(t)^k \rangle}$ and, in particular, the roughness $B(t) \equiv \overline{\langle y(t)^2 \rangle}$ with the roughness exponent $\zeta(t)$. We have recorded those quantities using a microscopic grid *linear* in t, and, in parallel for the roughness-related quantities, we have used a microscopic grid *logarithmic* in t in anticipation of power-law determination. Note that the even parity of the correlators has been explicitly used to

increase their statistics, so the measured $\bar{C}(t,y)$ and $\bar{R}(t,y)$ are symmetric by construction,

$$\bar{R}(t,y) = \tfrac{1}{2}\overline{[\partial_y \bar{F}(t,y)\,\partial_y \bar{F}(t,0) + \partial_y \bar{F}(t,-y)\,\partial_y \bar{F}(t,0)]},$$

$$\bar{C}(t,y) = \tfrac{1}{2}\overline{[\bar{F}(t,y) - \bar{F}(t,0)]^2 + [\bar{F}(t,-y) - \bar{F}(t,0)]^2}.$$

7. Fitting functions for $\bar{R}(t,y)$

The correlator $\bar{R}(t,y)$ is not known exactly at finite time, and, thus, we have only postulated its generic form $\bar{R}(t,y) \approx \widetilde{D}_t\,\mathcal{R}_{\tilde{\xi}_t}(y)$ in (20). Following the DP toy model assumption (20), we have systematically extracted the typical width $\tilde{\xi}_t$ and amplitude $\widetilde{D}_t$ for three different function $\mathcal{R}_{\tilde{\xi}}(y)$ with the chosen normalization $\int_{\mathbb{R}} dy\,\mathcal{R}_{\tilde{\xi}}(y) \equiv 1$. First, $\mathcal{R}_{\tilde{\xi}}(y)$ is taken to be a Gaussian function, whose single feature is given by its variance $2\tilde{\xi}^2$,

$$\mathcal{R}_{\tilde{\xi}}^{\mathrm{Gauss}}(y) = \frac{e^{-y^2/(4\tilde{\xi}^2)}}{\sqrt{4\pi}\,\tilde{\xi}}. \tag{35}$$

Second, we add phenomenologically two negative oscillations of the observed correlator by using a cardinal sinus of period $\tilde{\xi}/\pi$ with a Gaussian envelope function,

$$\mathcal{R}_{\tilde{\xi}}^{\mathrm{SincG}}(y) = e^{-y^2/(4\tilde{\xi}^2)}\,\frac{\sin[\pi y/\tilde{\xi}]}{\pi y\,\mathrm{Erf}(\pi)}. \tag{36}$$

And, third, we consider the same function as the exact two-point correlator of the microscopic random potential $\mathcal{R}_{\tilde{\xi}}^{\mathrm{CubicS}}(y) = R_{\tilde{\xi}}^{\mathrm{CubicS}}(y)$ defined in (A2) and (A3). $\{\tilde{\xi}_t, \widetilde{D}_t\}$ are reliable quantities if they do not depend on the choice of the fitting function, except for a numerical constant depending solely on the choice among $\mathcal{R}^{\mathrm{Gauss}}$, $\mathcal{R}^{\mathrm{SincG}}$, and $\mathcal{R}^{\mathrm{CubicS}}$. In Appendix A, we have compared the fit of the correlator $\overline{V(t,y)V(0,0)}$ with respect to $\mathcal{R}^{\mathrm{Gauss}}$, $\mathcal{R}^{\mathrm{SincG}}$, and $\mathcal{R}^{\mathrm{CubicS}}$ and determined the numerical constants for passing from one to the others as a consistency check of this procedure on this well-controlled correlator.

IV. TIME EVOLUTION OF $\bar{R}(t,y)$ AT FIXED TEMPERATURE

In this section we study in detail the time evolution of the correlator $\bar{R}(t,y)$ (16) at fixed temperature, from the point of view of our DP toy model (20). We thus focus on the evolution of its shape around $y = 0$, characterized by the effective parameters $\{\widetilde{D}_t, \tilde{\xi}_t\}$. Note that its behavior at large transverse displacements y has already been investigated from a different perspective in Ref. [41] on the equivalent correlator $\bar{C}(t,y)$ (15).

In Fig. 4 we have plotted the correlators at three characteristic temperatures $T \in \{0.35,1,6\}$, illustrating respectively the low-, intermediate-, and high-temperature regimes of the DP fluctuations; refer to Appendix B for the complete set of corresponding numerical parameters. We can follow the evolution of the correlator, starting by construction from the thermal condition $\bar{R}(t_0,y) \equiv 0$ at initial time $t_0 = 0.1$. At small times the central peak first increases but quickly saturates, and all the curves start accumulating in the vicinity of $y = 0$ (Fig. 4, left side). This behavior suggests qualitatively the existence of a saturation time t_{sat}. Assuming, thus, that at sufficiently large
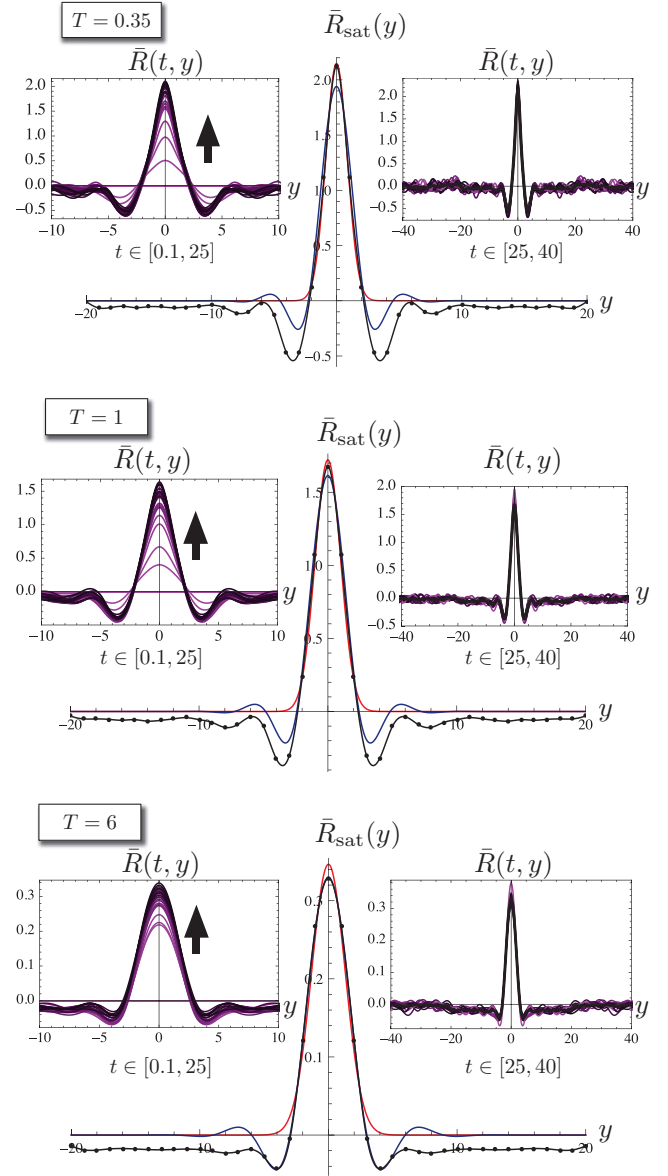

FIG. 4. (Color online) Effective disorder correlator $\bar{R}(t,y)$ measured numerically at fixed temperature $T \in \{0.35,1,6\}$. The different times $t \in [0.1,40]$ are separated into two subsets $[0,t_{\mathrm{min}}]$ (left) and $[t_{\mathrm{min}},40]$ (right) with $t_{\mathrm{min}} = 25$, with a time step $\Delta t = 1$. Left side ($y \in [-10,10]$): Initial development of the central peak (as indicated by the arrows), saturation, and accumulation of the curves in the vicinity of $y = 0$. Right side ($y \in [-40,40]$): Large times correlators and their average over $t > t_{\mathrm{min}}$ (superimposed black curve). Center: Saturation correlator $\bar{R}_{\mathrm{sat}}(y)$ (black dots) with its Gaussian (35) (red, positive) and SincG (36) (blue, with negative oscillations) fitting functions, CubicS collapsing exactly on SincG; see Table I in Appendix C for the explicit values of the fitting parameters.

times the correlator has reached its presumably stationary form at small y, the saturation correlator $\bar{R}_{\mathrm{sat}}(y)$ can be obtained by averaging the correlator over times larger than an arbitrary threshold $t_{\mathrm{min}} > t_{\mathrm{sat}}$ (Fig. 4, right side: superimposed black curve). This correlator can then be fitted according to (21) with respect to the three fitting functions $\mathcal{R}^{\mathrm{Gauss}}$, $\mathcal{R}^{\mathrm{SincG}}$, and $\mathcal{R}^{\mathrm{CubicS}}$ defined at the end of Sec. III B (Fig. 4, center). Having checked

that those results are stable for different values $t_{\min} > 10$, we have chosen arbitrarily $t_{\min} = 25$ for all temperatures in order to be safely above the saturation time $t_{\text{sat}} \lesssim 10$.

Therefore, we can distinguish two time regimes for the free-energy fluctuations just by considering $\bar{R}(t,y)$: (i) a short time evolution at $t < t_{\text{sat}}$, *a priori* marked by the artificial initial condition, and (ii) a saturation regime at $t \gtrsim t_{\text{sat}}$, when the correlator around $y = 0$ has reached a steady state and is described by the stable function $\bar{R}_{\text{sat}}(y) = \widetilde{D}_\infty \mathcal{R}_{\tilde{\xi}_\infty}(y)$, as assumed in our DP toy model (21). The linearized case (Fig. 2) and the three temperatures in Fig. 4 exhibit qualitatively the same two regimes. However, juxtaposing the high-, intermediate-, and low-temperature cases allows us to point out the slight temperature crossover in the *shape* of the asymptotic $\bar{R}_{\text{sat}}(y)$, which will be discussed in the next section.

An important point regarding the determination of $\bar{R}_{\text{sat}}(y)$ is that the large-y behavior of $\bar{R}(t,y)$ is treated as noise in the averaging procedure. From the point of view of our DP toy model (20), this is equivalent in neglecting the negative excursions $b(t,y)$ in (25) or in the linearized case (24), which are known to move to larger y with increasing time [41]. It results in a slight displacement below the abscissa axis of the large-y asymptote of $\bar{R}_{\text{sat}}(y)$. We have to cope with this artifact, present in all three temperatures in Fig. 4, since we do not know analytically $b(t,y)$ for a correlated disorder ($\xi > 0$) and, thus, we cannot remove its contribution before averaging over large times.

In order to characterize quantitatively the two time regimes of the free-energy fluctuations, we have measured the evolution of the two fitting parameters $\{\widetilde{D}_t, \tilde{\xi}_t\}$ by the bold application of the approximation $\bar{R}(t,y) \approx \widetilde{D}_t \mathcal{R}_{\tilde{\xi}_t}(y)$ of our DP toy model (20) at all times. We refer the reader to Appendix C for a detailed quantitative comparison of the three fitting procedures with respectively $\mathcal{R}^{\text{Gauss}}$, $\mathcal{R}^{\text{SincG}}$, and $\mathcal{R}^{\text{CubicS}}$ for the three characteristic temperatures of Fig. 4. This quantitative comparison shows that (i) the approximation of our DP toy model (20) can be extended even at times shorter than t_{sat}, as the fitting parameters can be obtained with reasonable uncertainties for the low- versus high-temperature fits (see Figs. 11 and 12 in Appendix C), and (ii) the three fitting functions for $\mathcal{R}(y)$ yield consistent values for $\{\widetilde{D}_t, \tilde{\xi}_t\}$ and their discrepancies allow us to characterize the temperature crossover of the correlator's shape (see Fig. 13 in Appendix C).

As shown in Fig. 5 for increasing temperatures (blue to red curves), we can clearly identify the two regimes of short time versus saturation directly on these fitting parameters. The saturation is reached faster for the typical spread $\tilde{\xi}_t$ than for the amplitude $\widetilde{D}_t$, with t_{sat} slightly decreasing when the temperature increases. On the temperature range we explore numerically, we have $t_{\text{sat}} \lesssim 10$, as already deduced from Fig. 4. The temperature dependence of the asymptotic correlator $\bar{R}_{\text{sat}}(y)$ thus can be safely obtained from averaging over times $t > t_{\min} = 25$ and will be discussed in the next section.

As a concluding remark, let us emphasize that the temperature crossover of $\{\widetilde{D}_\infty, \tilde{\xi}_\infty, \mathcal{R}\}$ is conditioned by the short time regime and thus requires a deeper understanding of the KPZ nonlinearity feedback at times $t < t_{\text{sat}}$. Nevertheless, in our numerical measurements, these short times are *a priori* altered by the artificial initial condition, whose signature has thus to
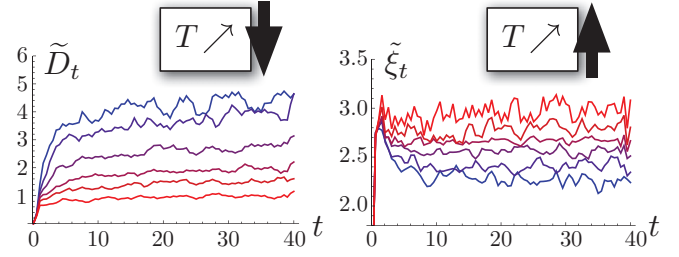

FIG. 5. (Color online) Temperature-dependent amplitude $\widetilde{D}_t$ and typical spread $\tilde{\xi}_t$ for SincG for $T \in \{0.35, 1, 2, 3, 4, 6\}$ as listed in Appendix B. See Appendix C 1 for the error bars of the minimum and maximum temperatures. For increasing temperatures (blue to red), $\widetilde{D}_t$ decreases, whereas $\tilde{\xi}_t$ slightly increases ($\xi_y^{\text{grid}} = 2$ for reference), resulting in an overall damping of the correlator $\bar{R}_{\text{sat}}(y)$ (see Fig. 6).

be investigated otherwise, via the roughness in Sec. VI or the study of $\partial_t \overline{F_V}(t,y)$ in Appendix D.

V. TEMPERATURE DEPENDENCE OF $\bar{R}_{\text{sat}}(y)$

In the previous section, we have discussed the time evolution of the correlator $\bar{R}(t,y)$ (15) and pointed out the existence of a characteristic time t_{sat} that separates a short-time regime from a saturation regime. Now we focus on the temperature dependence of the large-time free-energy fluctuations in order to observe numerically the crossover from the high- to the low-temperature regime, as predicted analytically when the microscopic disorder is correlated with $\xi > 0$ [40,42] (see Sec. II B).

From the point of view of our DP toy model (21), we examine the saturation correlator $\bar{R}_{\text{sat}}(y)$, discussing on one hand the crossover in the shape $\mathcal{R}(y)$ of its central peak and on the other hand the temperature dependence of its fitting parameters, i.e., the amplitude $\widetilde{D}_\infty$ and typical spread $\tilde{\xi}_\infty$ of the correlator.

In Fig. 4 we have plotted $\bar{R}_{\text{sat}}(y)$ and its fits with respect to the three functions $\mathcal{R}(y)$ at low, intermediate, and high temperatures (center). We observe graphically that at high T the exact microscopic disorder correlator $\mathcal{R}^{\text{CubicS}}(y)$ or, alternatively, its phenomenological counterpart $\mathcal{R}^{\text{SincG}}(y)$ both correctly encompass the features of the whole peak, including its maximum and its negative anticorrelations. At low T, on the contrary, $\mathcal{R}^{\text{Gauss}}(y)$ appears to be more suited to capture the central peak and its maximum, although completely skipping its anticorrelations. These anticorrelations are obviously inherited from the microscopic disorder correlator $R_\xi(y) = \mathcal{R}_\xi^{\text{CubicS}}(y)$, plotted in Fig. 10 in Appendix A. They are, however, progressively altered when the temperature is lowered. As for the negative shift of the large-y asymptote, it is an expected artifact of the averaging procedure (see Sec. IV), and as such it is not encompassed by any of the fitting functions $\mathcal{R}(y)$.

This behavior suggests that at high T the imprint of the microscopic disorder correlator is recovered in the asymptotic shape $\mathcal{R}(y)$, as it is exactly the case at infinite time for an uncorrelated disorder (22) and for the linearized case with $\xi > 0$ (23). At low T the shape is analytically not known, but we speculate that it could be a convolution of the disorder

correlator $R_\xi(y)$ and a universal kernel, yielding a modified (nonuniversal) Airy kernel in (17). Note that this effect would actually have gone unnoticed if we had focused directly on the parameters $\{\widetilde{D}_t, \widetilde{\xi}_t\}$ or if we had considered the correlator $\bar{C}(t,y)$ (15) instead of $\bar{R}(t,y) = \frac{1}{2} \partial_y^2 \bar{C}(t,y)$.

We have furthermore characterized quantitatively this temperature crossover in Appendix C, on one hand, by computing the geometrical ratios $\frac{\widetilde{D}_\infty^{\mathrm{SincG}}}{\widetilde{D}_\infty^{\mathrm{Gauss}}}$ and $\frac{\widetilde{\xi}_\infty^{\mathrm{SincG}}}{\widetilde{\xi}_\infty^{\mathrm{Gauss}}}$ (see Appendix C 1) and, on the other hand, by comparing the maximum of the peak $\bar{R}(t,0)$ to the values deduced from the different fits (see Appendix C 2). Both analyses support quantitatively the high-T scenario of $\mathcal{R}(y) \approx \mathcal{R}^{\mathrm{CubicS}}(y)$.

We now consider the temperature dependence of the amplitude $\widetilde{D}_\infty$, which is the central quantity controlling the temperature crossover at $\xi > 0$ in our analytical predictions [42], both for the free energy and the geometrical fluctuations [see respectively (17), (18) and (30)]. In Fig. 5 we observe graphically that the amplitude $\widetilde{D}_\infty$ decreases strongly with T, whereas the typical spread $\widetilde{\xi}_\infty$ increases (up to 30%) when T increases. These behaviors result in an overall damping of the effective disorder correlator $\bar{R}_{\mathrm{sat}}(y)$ when the thermal fluctuations are enhanced, as plotted in the inset of Fig. 6. Comparing quantitatively the values obtained for the three fitting functions $\mathcal{R}(y)$ in Appendix C 3, we find that $\widetilde{D}_\infty(T)$ exhibits a monotonous crossover from $1/T$ at high T to a saturation $1/T_c(\xi)$ at low T. This behavior is qualitatively consistent with the GVM prediction presented after (19), but a quantitative test is hindered by numerical constants inherent on

one hand to our numerical procedure and on the other hand to the GVM approximation. The corresponding $\widetilde{\xi}_\infty(T)$ displays in parallel a slight temperature dependence that either corrects the minimal assumption $\widetilde{\xi}_\infty \propto \xi$ of our DP toy model or can be attributed to the mismatch between $\mathcal{R}(y)$ and our fitting functions.

We summarize all these temperature dependencies in Fig. 5, plotting $\bar{R}_{\mathrm{sat}}(0) \sim \widetilde{D}_\infty/\widetilde{\xi}_\infty$ as a function of T. The main result of our numerical study is the observation of the temperature crossover of the amplitude $\widetilde{D}_\infty$, and, hence, of $\bar{R}_{\mathrm{sat}}(0)$, and their saturation below a characteristic temperature T_c. We actually compare four distinct determinations of this quantity: (i) a direct measurement on $\bar{R}_{\mathrm{sat}}(y)$, (ii) the values obtained from $\mathcal{R}^{\mathrm{Gauss}}(y)$, (iii) the values obtained from $\mathcal{R}^{\mathrm{CubicS}}(y)$ and $\mathcal{R}^{\mathrm{SincG}}(y)$ which collapse exactly, and (iv) and an alternative measurement via $\partial_t \bar{F}_V(t,y)$ which is presented in Appendix D. By their good quantitative agreement, this comparison provides a consistency check of our numerical procedure and an additional highlight of the temperature crossover of the correlator shape $\mathcal{R}(y)$. The crossover temperature cannot be sharply determined from $\bar{R}_{\mathrm{sat}}(0)$; nevertheless, the definition $T_c(\xi) = (\xi c D)^{1/3}$ obtained by GVM [40] and by scaling arguments [42] predicts with $\xi = 2$, $c = 1$, and $D = 8$ that $T_c \approx 2.5$. Without any corrective numerical constant this value is actually compatible with the crossover of the amplitude $\widetilde{D}_\infty(T,\xi)$ in Fig. 14 and also of the function $\mathcal{R}(y)$ in Fig. 13 (bottom left).

VI. TEMPERATURE DEPENDENCE OF THE ROUGHNESS FUNCTION $B(t)$

Until now we have analyzed in detail the disorder free-energy fluctuations from the point of view of our DP toy model [(20) and (21)], i.e., characterizing specifically the two-point correlator $\bar{R}(t,y)$ (16). Keeping in mind the translation of the time t for the DP end point into the 1D interface length scale, we focus now on the implications of t_{sat} and $\widetilde{D}_\infty$ in the geometrical fluctuations. We examine specifically their variance as a function of time, namely the roughness $B(t) = \overline{\langle y(t)^2 \rangle}$ as presented in Sec. II C.

As recalled in Sec. II after the definition (28), the roughness is expected to display at least two asymptotic power-law regimes (30), crossing from a pure thermal behavior $B(t) \gtrsim B_{\mathrm{th}}(t) = \frac{Tt}{c}$ at short times to the random-manifold $B_{\mathrm{RM}}(t) \sim [\widetilde{D}_\infty/c^2]^{2/3} t^{4/3}$ at large times. Above T_c there is a single crossover Larkin time $t_*(T) = \frac{T^5}{cD^2}$ corresponding to the intersection of the two asymptotic regimes of (30). This length diverges with T and essentially prevents us from observing the complete crossover to the RM regime in our numerical approach in a reasonable computational time for $T > 2$. Below T_c, however, we expect from Ref. [40] the appearance of an intermediate Larkin-modified roughness regime ending at the generalized Larkin time $L_c(T,\xi)$

$$L_c(T,\xi) = 4\pi \frac{T^5}{cD^2} f(T,\xi)^{-5}, \tag{37}$$

which marks the beginning of the RM regime, cf. Sec. II C. It depends on the interpolating parameter $f(T,\xi) = \widetilde{D}_\infty/(\frac{cD}{T})$ defined in (19) and which characterizes the crossover between
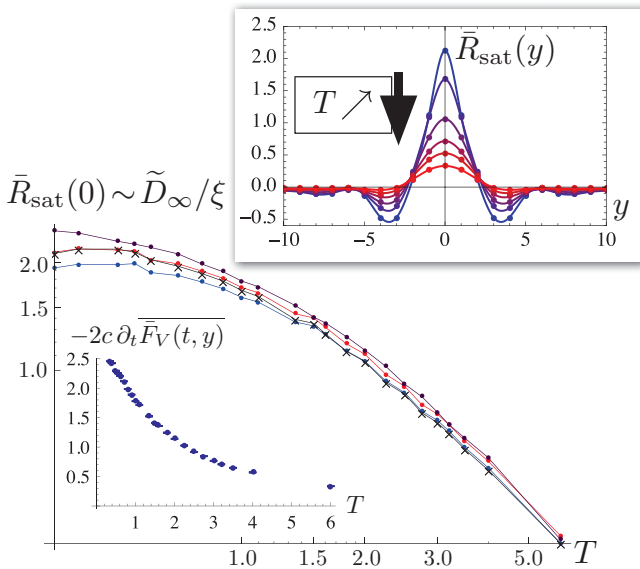

FIG. 6. (Color online) Temperature dependence of the maximum of $\bar{R}_{\mathrm{sat}}(y)$ over times $t \in [25,40]$, measured by three different ways (from bottom to top): first, deduced by the SincG and Gauss fits as in Fig. 13 (respectively, blue and red dots); second, measured numerically directly $\bar{R}_{\mathrm{sat}}(0)$ (black crosses); and, third, measured indirectly from the linear slope of $-2c\,\bar{F}_V(t,y)$ in Fig. 16 (purple dots) and systematically slightly overestimated. Upper inset: Saturation correlator $\bar{R}_{\mathrm{sat}}(y)$ for temperatures $T \in \{0.35,1,2,3,4,6\}$ (as indicated by the arrow) and $t_{\mathrm{min}} = 25$ as listed in Appendix B. Lower inset: The excellent linear behavior of $\bar{F}_V(t,y)$ yields vanishing error bars for the slope on the range $t \in [25,40]$.

the high- and low-temperature regimes [42]. In order to understand how the intermediate Larkin-modified regime appears, we focus on the pure disorder component of the roughness,

$$B_{\text{dis}}(t) = B(t) - \frac{Tt}{c} = \overline{\langle y(t)^2 \rangle}^c \qquad (38)$$

(this equality is a consequence of the STS [42,49–51]). We will argue that the two-time regimes of $\bar{R}(t, y)$, separated by t_{sat}, are actually transposed to $B_{\text{dis}}(t)$: The competition between $B_{\text{th}}(t)$ and $B_{\text{dis}}(t)$ then yields two or three roughness regimes, respectively, at high T and at low T. In particular, the Larkin time is reached when $B(t) \approx B_{\text{dis}}(t) \approx B_{\text{RM}}(t)$, implying that $t_{\text{sat}} \lesssim L_c$.

Although the GVM framework yields a prediction for the full temperature crossover of the DP toy model (see, e.g., Ref. [40] and Appendix A of Ref. [42]), a complete *quantitative* test of this prediction is hindered by the numerical constants that are *a priori* present in the determination of $\widetilde{D}_t$, $\tilde{\xi}_t$, T_c, and L_c and the amplitude of the asymptotic roughness itself, due to previously discussed numerical artifacts and also to the GVM approximation. Nevertheless, we observe *qualitatively* these different roughness regimes, as plotted at fixed temperature $T \in \{0.35, 1, 1.8\}$ in Fig. 7, indicating both the total roughness $B(t) = \overline{\langle y(t)^2 \rangle}$ and its pure disorder component. In all three graphs we can follow the crossover in time from the thermal asymptote to the RM asymptote which stems from the increasing $B_{\text{dis}}(t)$ added to $B_{\text{th}}(t)$. Note that the RM asymptote has been constructed consistently with (30) with a numerical correction fixed once and for all, from the data set $T = 0.4$ averaged over $t \in [25, 40]$, assumed to be already in the RM regime,

$$\frac{B_{\text{RM}}(t)}{t^{4/3}} \approx \text{corr}_{(T=0.4)} \frac{3}{2^{2/3} \pi^{1/3}} \left[\frac{\widetilde{D}_\infty^{\text{SincG}}(T, \xi)}{c^2} \right]^{2/3}, \quad (39)$$

with $\text{corr}_{(T=0.4)} = 0.292 \pm 0.008$. This RM asymptote is graphically consistent with all the available data sets in the range $T \in [0.35, 1.8]$, which plays in favor of a numerical corrective factor common to all temperatures and absorbing the discrepancy in $B_{\text{RM}}(t)$ stemming from $\widetilde{D}_\infty$ and the GVM. The low-T regime is illustrated by $T = 0.35$ where the intermediate Larkin-modified regime is clearly present, whereas it has disappeared as such already at $T = 1$.

We are limited, in our numerical procedure, in the large times that we can explore in a reasonable computation time. Larger times have, however, been explored at $T = 1.8$, which is believed to be close to T_c (cf. Sec. V) and is consistent with lower temperatures, except for a sudden increase at $t > 400$, which can clearly be attributed to the finite size of the box $y \in [-y_m, y_m]$. Confining effects due to the finite box $[-y_m, y_m]$ do not appear until $\sqrt{B(t)} \sim y_m$, and this condition translates for this data set into $B(t) < 160^2 = 2.5 10^4$ and yields an adequate upper bound in Fig. 7 (bottom). The corresponding upper bound for most of the data sets is $B(t) < 40^2 = 160$, consistent with the range of roughness displayed in all the other graphs.

Gathering in Fig. 8 the roughness $B(t)$ and $B_{\text{dis}}(t)$ over the range $T \in [0.35, 6]$, we observe, as expected with increasing temperature, that the disorder roughness $B_{\text{dis}}(t)$ is
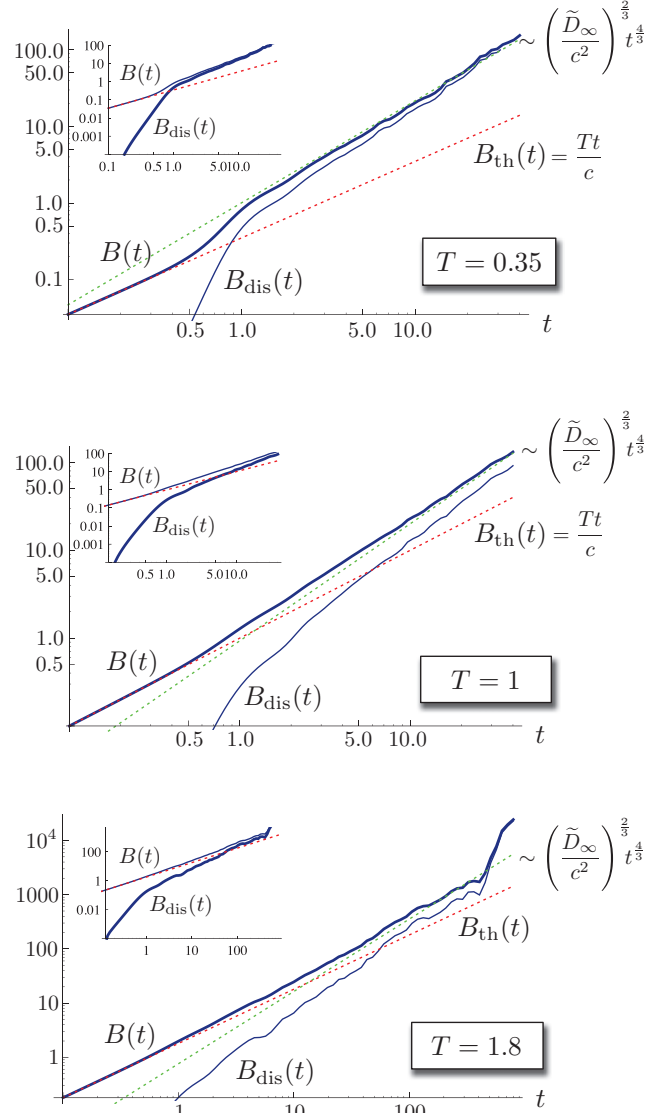

FIG. 7. (Color online) Roughness $B(t) = \overline{\langle y(t)^2 \rangle}$ and its disorder component $B_{\text{dis}}(t) = B(t) - \frac{Tt}{c} = \overline{\langle y(t)^2 \rangle}^c$ measured numerically at fixed temperature $T \in \{0.35, 1, 1.8\}$. Main: Focus on the crossover of $B(t)$ (thick) from the pure thermal behavior $B_{\text{th}}(t) = \frac{Tt}{c}$ (dotted red) at short times to the asymptotic $B_{\text{RM}}(t) \sim \widetilde{D}_\infty(T)^{2/3} t^{4/3}$ (dotted green) at asymptotically large times; $B_{\text{dis}}(t)$ is the thinner lower curve. Inset: Focus on the short-times crossover of $B_{\text{dis}}(t)$ (thick) in parallel to $B(t)$ (thin).

progressively damped by thermal fluctuations. The intermediate Larkin-modified regime thus shrinks with increasing temperature. The beginning of the RM regime is, consequently, pushed to larger times, as it could also be deduced by the condition that $B_{\text{dis}}(t)$ becomes comparable to $B_{\text{th}}(t)$ close to the Larkin time $t = L_c$. From the point of view of the 1D interface, the temperature dependence of $B_{\text{dis}}(t)$ can be physically understood with the following picture: At small length scales the thermal fluctuations make the interface rougher within the local valleys of the disordered free-energy landscape and $B(t) \gtrsim B_{\text{th}}(t)$ increases with T as expected; and at large length scales, on the contrary, thermal fluctuations allow the interface to explore more effectively the free-energy landscape by
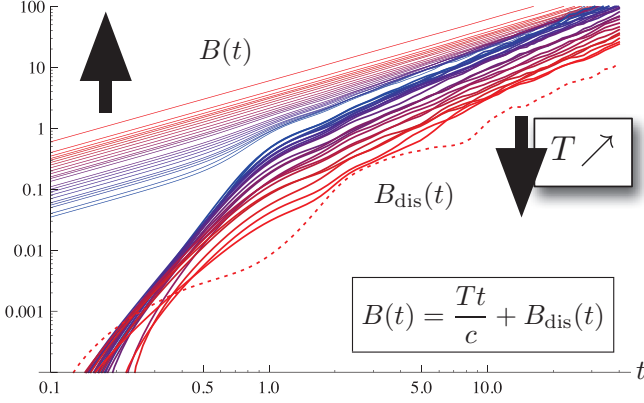
FIG. 8. (Color online) Temperature-dependent roughness $B(t) = \overline{\langle y(t)^2 \rangle}$ and its disorder component $B_{dis}(t)$ (in logarithmic scale, respectively, the top and bottom curves) for $T \in [0.35, 6]$ as listed in Appendix B (blue to red for increasing temperatures, as indicated by the black arrows). $B_{dis}(t)$ for $T = 6$ is indicated in dotted red. See Fig. 7 for the description of the different regimes for three fixed temperatures.

FIG. 9. (Color online) Logarithmic slope of the roughness, $\zeta(t)$ and $\zeta_{dis}(t)$, obtained, respectively, from $B(t)$ and $B_{dis}(t)$ of Fig. 8 for $T \in [0.35, 1]$ (blue to red for increasing temperatures, as indicated by the black arrow) and $T = 1.8$ (in thin dashed dotted black). The thermal exponent $\zeta_{th} = \zeta_{EW} = \frac{1}{2}$ and the RM exponent $\zeta_{RM} = \zeta_{KPZ} = \frac{2}{3}$ are indicated by the thick dash-dotted lines, respectively red and green. At larger times those logarithmic slopes are very noisy but still oscillate around the expected value $\zeta_{RM} = \frac{2}{3}$.

overcoming some free-energy barriers in order to minimize its elastic energy and, thus, have $B_{RM}(t)$ decreasing with T. From the point of view of the DP, these behaviors are encoded in the evolution of the translation-invariant distribution $\overline{\mathcal{P}}[\bar{F}, t]$ (13), the integration of the microscopic disorder $V(t', y')$ explored by the elastic DP over times $[0, t]$ defining the effective disorder $\bar{F}_V(t, y)$, or, equivalently, in the moments $\overline{\langle y(t)^k \rangle}$ of the DP end point. The saturation at low T of the amplitude $\widetilde{D}_\infty$ in Fig. 14 and of the peak $\bar{R}(t, 0)$ in Fig. 6 naturally translates into a saturation of the asymptotic amplitude of the roughness (39).

In order to focus on the disorder contribution, we computed numerically directly $\bar{F}_V(t, y)$, but, regarding the roughness, we had to, first, construct the total free energy $F = F_{th} + \bar{F}$ and then compute the total roughness $B(t)$ and eventually deduce its disorder component, $B_{dis} = B - B_{th}$. This quantity is, thus, more subject to noise at higher T (see, i.e., $T = 6$ in Fig. 8), but, especially at low T, it clearly displays two regimes in time. To address the question of a possible power law at short times, the logarithmic slope $\zeta_{(dis)}(t) = \frac{1}{2} \frac{\partial B_{(dis)}(t)}{\partial \log t}$ is plotted in Fig. 9. While $\zeta(t)$ crosses over as expected from $\zeta_{th} = \zeta_{EW} = \frac{1}{2}$ to $\zeta_{RM} = \zeta_{KPZ} = \frac{2}{3}$ (30) but excludes the definition of an intermediate-time power law for $B(t)$, $\zeta_{dis}(t)$, on the contrary, displays a plateau at low T which disappears at $T = 1$, a tendency confirmed at $T = 1.8$. According to the GVM prediction [40], $B_{dis}(t)$ should start in $\sim \frac{\widetilde{D}}{c^2} t^2 / \tilde{\xi}$, in which case the value of the plateau would have 1 as a lower band and only a time dependence of $\widetilde{D}_t$ and/or $\tilde{\xi}_t$ could correct ζ_{dis} to match the GVM prediction. This results is not to be trusted *a priori* at times shorter than L_c [42]. The value of this plateau exhibits, moreover, a slight temperature dependence, which cannot be accounted for by our DP toy model but might also simply be an artifact of the thermal condition imposed at $t_0 = 0.1$. Note, finally, that all these effects on $B_{dis}(t)$ take place before $t_{sat} \lesssim 10 < L_c$, as estimated on the saturation of the free-energy correlator $\bar{R}(t, y)$ in the previous sections.
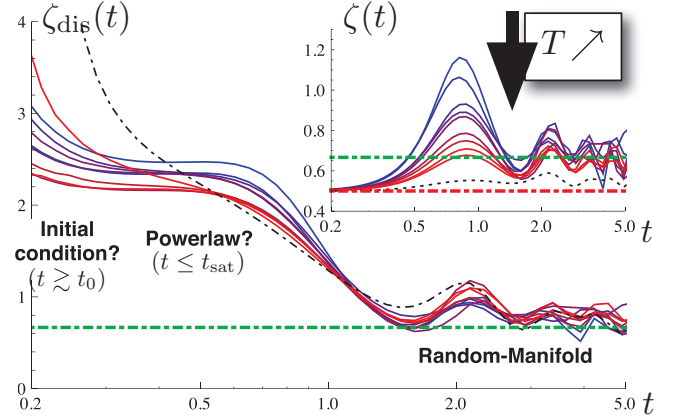
VII. CONCLUSION

In this paper, we have studied numerically the free-energy and geometrical fluctuations of a $1 + 1$ DP growing in a quenched disordered energy landscape, uncorrelated in the time direction and with a finite disorder correlation length ξ in the transverse direction y as given in (3). This model actually yields an effective description of the static 1D interface fluctuations at fixed length scale, which translates into the DP growing time. We have specifically characterized the fluctuations of the disorder free energy $\bar{F}(t, y)$ defined by (10)–(12), focusing on one hand on its two-point correlator $\bar{R}(t, y) = \partial_y \bar{F}_V(t, y) \partial_y \bar{F}_V(t, 0)$ and its mean value $\overline{\bar{F}_V(t, y)} = -\frac{1}{2c} \int_0^t dt' \, \bar{R}(t', 0)$ and on the other hand on its consequent geometrical fluctuations, via the roughness function $B(t)$. Our numerical procedure amounts to the integration of the KPZ equation for the total free energy (8) with a "sharp-wedge" initial condition and a colored noise of correlator $R_\xi^{CubicS}(y)$, resulting from a cubic-splined interpolation of the random potential (as presented in Appendix A).

We have, first, successfully tested the main assumption of our DP toy model at the core of the analytical study in Ref. [42] and the GVM roughness computations [18,40]: At small transverse displacements y the correlator behaves as $\bar{R}(t, y) \approx \widetilde{D}_t \, \mathcal{R}_{\tilde{\xi}_t}(y)$, consistently with three different fitting functions for $\mathcal{R}(y)$ in Sec. IV, respectively, $\mathcal{R}^{Gauss}$ (35), $\mathcal{R}^{SincG}$ (36), and $\mathcal{R}^{CubicS}$ [(A2) and (A3)]. We have clearly identified two time regimes in the evolution of the free-energy fluctuations: a short-time regime where the correlator starts from its initial flat condition and grows while integrating the interplay between the disorder correlation and thermal fluctuations that intervenes precisely at small length scale y; and a large-time regime above a saturation time t_{sat} where the correlator is well approximated locally by its asymptotic limit $\widetilde{D}_\infty \, \mathcal{R}_{\tilde{\xi}_\infty}(y)$ and, thus, keeps track of the short-time evolution from t_{sat} up to the macroscopic scale. The combination between

the disorder free energy $\bar{F}_V(t,y)$ and the thermal free energy $F_{\text{th}}(t,y)$ leads to two or three regimes for the roughness $B(t)$, respectively, at high or low temperature with respect to the characteristic temperature $T_c(\xi) = (\xi c D)^{1/3}$. A simpler physical picture is, however, regained by focusing on the disorder roughness $B_{\text{dis}}(t) = B(t) - B_{\text{th}}(t)$, which displays the same two time regimes as the disorder free energy (see Fig. 8).

We have, second, followed the temperature dependence of the large-time DP fluctuations, whose amplitudes are found in qualitative agreement with the analytical predictions of our companion paper [42]. On one hand, we have multichecked that the free-energy amplitude $\widetilde{D}_\infty \sim \bar{R}(t,0)\tilde{\xi}_\infty$ crosses over monotonously from the high-temperature limit $\widetilde{D}_\infty \sim 1/T$ to the low-temperature saturation $\widetilde{D}_\infty \sim 1/T_c(\xi)$ (see Fig. 6), and, on the other hand, that this crossover matches the temperature dependence of the asymptotic roughness $B_{\text{RM}}(t) \sim \widetilde{D}_\infty^{2/3} t^{4/3}$ (see Fig. 7). Although numerical constants stemming from the analytical approximations or from the numerical procedure clearly hinder a quantitative test, these results support a universality scenario for the amplitudes. Consequently, even though ξ might lie below accessible resolution in physical systems, it can still play a role at all length scales below $T_c(\xi)$ (including scales much larger than ξ itself) and, hence, proves experimentally relevant. In other words, if the temperature dependence of the parameters $\{c,D,\xi\}$ is known, changing the temperature amounts to the exploration of the disorder spatial correlation: The details of the random potential are probed with the thermal fluctuations. This conclusion is, thus, encouraging to study the temperature dependence of experimental systems, such as the magnetic domains walls or interfaces in liquids crystals as discussed in Ref. [42].

Beyond the universal large-scale exponent $\zeta_{\text{KPZ}} = \frac{2}{3}$ and the universal crossover of the amplitude $\widetilde{D}_\infty(T,\xi)$, we believe that the precise shape $\mathcal{R}(y)$ also displays universality, in the form of a universal kernel that combines with the specific microscopic disorder correlator $R_\xi(y)$ in order to yield a generalized Airy$_2$ process (17). This guess is supported analytically by the $\xi = 0$ limit (22) and the linearized case (23) and numerically by an increasing discrepancy between $\mathcal{R}(y)$ and $R_\xi^{\text{CubicS}}(y)$ as the temperature is lowered. The imprint of the microscopic disorder on the macroscopic fluctuations of the $1 + 1$ DP, or the static 1D interface, is numerically such that at high temperature $\mathcal{R}(y) \approx R_\xi^{\text{CubicS}}(y)$, whereas at low temperature it displays a better agreement with $R_\xi^{\text{Gauss}}(y)$. The determination of the zero-temperature limit of $\mathcal{R}(y)$, let alone its complete temperature dependence, remains an open question analytically and will require a complete understanding of the non-Gaussian features of the free-energy fluctuations and the role of the KPZ nonlinearity in (14). To tackle this issue numerically will require a better characterization of the short-time free-energy fluctuations and in particular of the initial-condition signature in $\{\widetilde{D}_t, \tilde{\xi}_t\}$, $\partial_t \bar{F}_V(t,y)$, and $B_{\text{dis}}(t)$.

To summarize, systems belonging to the KPZ universality class are characterized not only by the large-scale exponent $\zeta_{\text{KPZ}} = \frac{2}{3}$ but also by universal *distributions* and universal *amplitudes*. The high-temperature limit of the amplitude $\widetilde{D}_\infty = \frac{cD}{T}$ is known from the generic KPZ scaling theory (see Refs. [33,34] for reviews), while the crossover to lower temperatures seems to be new, even at the numerical level. We suspect that the anomaly observed numerically in Ref. [64] for the free-energy amplitude $\widetilde{D}_\infty$ with respect to the expected scaling is an effect due to a small correlation length of the disordered potential that was not taken into account since $\widetilde{D}_\infty$ was compared to its zero ξ (i.e., high-temperature) expression. Another situation where our results might prove relevant is that of the last-passage percolation [24], which is a "zero-temperature" discrete DP on a lattice: The problem amounts to finding a path with minimal energy, which, in our framework, corresponds to a situation where both ξ and T are equal to 0 in the macroscopic limit. In the continuum formulation, those two limits do not commute, so a correct scaling limit remains to be found, and our findings indicate that the lattice spacing might induce observable evidences at large scale.

From a broader perspective, our numerical procedure provides a new computation frame for the continuous $1 + 1$ KPZ equation (8) with a "sharp-wedge" initial condition, which allows us to study the interplay of a colored noise with the KPZ nonlinearity, whose resulting feedbacks generate new phases compared to the white-noise case. Last, note that if the two temperature regimes can be hinted by scaling arguments [18], the question of relating those to possible two opposite functional renormalization group regimes of high temperature [56] versus a zero-temperature fixed point [65,66] remains open. In the case of DP in higher dimensionalities, as recently studied exhaustively in Ref. [67], one might also expect manifestations of the disorder correlation length ξ at low-enough temperatures.

APPENDIX A: EFFECTIVE CORRELATOR OF A 2D CUBIC-SPLINED MICROSCOPIC DISORDER

As described in Sec. III, a given configuration of the microscopic disorder $V(t,y)$ is generated, first, by picking up a set of random numbers $\{V_j\}$ on a grid of spacing $\{\xi_t^{\text{grid}}, \xi_y^{\text{grid}}\}$ with a normal distribution of variance D^{grid} and then by interpolating between the grid points with a 2D cubic spline (cf. Fig. 10, top).

In the reduced case of a 1D cubic spline between a set of points at a fixed position t on the grid, it is possible to determine analytically the effective correlator of the 1D cubic-splined random potential with a normalized function $R_{\xi_y}^{\text{CubicS}}(y)$ [cf. (3)]. For the 2D spline we then assume that the effective two-point disorder correlator is given by the translation invariant,

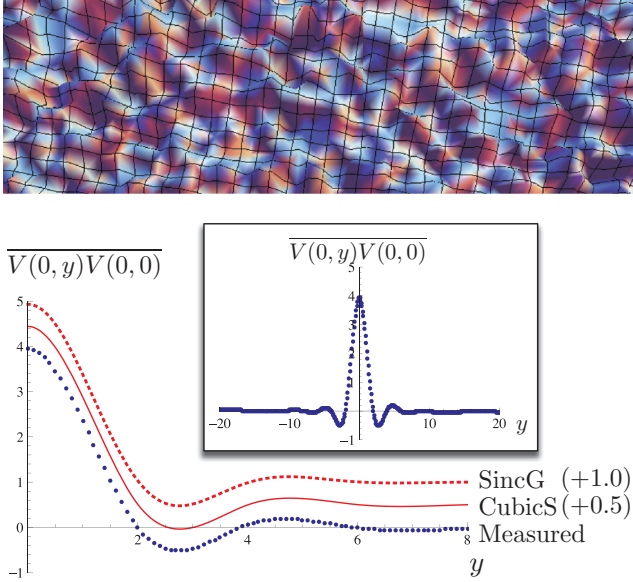$$\overline{V(t,y)V(0,0)} = D\, R_{\xi_t}^{\text{CubicS}}(t)\, R_{\xi_y}^{\text{CubicS}}(y), \qquad \text{(A1)}$$

FIG. 10. (Color online) Top: Visualization of a single disorder configuration $V(t,y)$; the mesh accounts for the grid $\{y_j\}$ and fluctuates smoothly. Bottom: Graph of the numerically measured effective 1D cubic-splined disorder correlator (blue), with the SincG and CubicS (red, respectively dashed and continuous) superimposed with a slight translation for more visibility. Inset: Full effective disorder correlator at fixed $t = 0$ computed over 10 000 disorder configurations with $D^{\text{grid}} = 4$, $\xi_y^{\text{grid}} = 2$, and $\xi_t^{\text{grid}} = 1$.

with $\xi_t = \xi_t^{\text{grid}}$ and $\xi_y = \xi_y^{\text{grid}}$ by construction and, because of the passage from the discretized y_j to the continuous variable y, an amplitude $D = D^{\text{grid}}\xi_t^{\text{grid}}\xi_y^{\text{grid}}$.

In practice, for $2n + 1$ points indexed by $j = -n, \ldots, n$ on a grid of spacing ξ, a random value V_j is attached on each site $y_j = j\xi$ of the grid following the statistical distribution $\overline{V_j} = 0$ and $\overline{V_j V_{j'}} = \delta_{jj'}$. A cubic spline of $\{V_j\}_{-n \leqslant j \leqslant n}$ is a function $V(y)$ which is a cubic polynomial on each lattice segment $y \in [y_j, y_{j+1}]$, continuous on each lattice site y_j and with its first and second derivatives also continuous at $y = y_j$. Combining the equations of the cubic-splined parameters for a given set $\{V_j\}$ and the disorder average over those possible sets, we obtain the following *symmetric* effective correlator in the limit of $n \to \infty$:

$$R_\xi^{\text{CubicS}}(0 \leqslant y \leqslant \xi)$$
$$= -\frac{1}{\xi^4}(y - \xi)[(4 - 3\sqrt{3})y^2 + \xi y + \xi^2], \quad \text{(A2)}$$

$$R_\xi^{\text{CubicS}}(y_j \leqslant y \leqslant y_{j+1})$$
$$= -\frac{3}{\xi^4}(y - y_j)(y - y_{j+1})(\sqrt{3} - 2)^j$$
$$\times [y - y_{j-1} - \sqrt{3}(y - y_j)], \quad \text{(A3)}$$

where there is a distinction between the central segment $0 \leqslant y \leqslant \xi$ which contains the autocorrelation

$$R_\xi^{\text{CubicS}}(y = y_{j=0}) = \overline{V_0^2} = \overline{V_j^2} = 1$$

and the other segments $y_j \leqslant y \leqslant y_{j+1}$ $(j = 1 \cdots n)$ with oscillations constrained by the cancellation at $y = y_{j \neq j}$,

$$R_\xi^{\text{CubicS}}(y = y_{j \neq 0}) = \overline{V_0 V_{j \neq 0}} = 0.$$

Note that this correlator has been obtained exactly by averaging over disorder the cubic splines, whose coefficients depend *linearly* in the random potential and, thus, allow an analytical computation of this average.

For the microscopic disorder correlator (A1) the function R_ξ is, thus, exactly known, but it is not the case for the effective disorder in our DP toy model [(20) and (21)] approximating $\bar{R}(t,y) = \overline{\partial_y \bar{F}_V(t,y) \, \partial_y \bar{F}_V(t,0)}$. As explained in Sec. III, we try nevertheless to extract the effective parameters at fixed time $\{\widetilde{D}_t, \widetilde{\xi}_t\}$ with three different fitting functions normalized to 1: (i) a Gaussian (35) (Gauss), (ii) a sinus cardinal with a Gaussian envelope (36) (SincG), and (iii) the exact cubic-spline correlator [(A2) and (A3)] (CubicS). The comparison between those three options accounts for a consistency check for the determination of the effective parameters via the stability of the function. We first test this procedure on $\overline{V(t,y)V(0,0)}$ (A1) by fitting this correlator separately at fixed time $t = 0$ versus at fixed position $y = 0$,

$$\overline{V(t,0)V(0,0)} = [D \, R_{\xi_y}(0)] \, R_{\xi_t}(t) \propto R_{\xi_t}(t),$$
$$\overline{V(0,y)V(0,0)} = [D \, R_{\xi_t}(0)] \, R_{\xi_y}(y) \propto R_{\xi_y}(y), \quad \text{(A4)}$$

we summarize thereafter the values obtained for the amplitude D and the correlation lengths $\xi_{t,y}$ with respect to the grid parameters (which are kept at fixed value throughout all our computations). The errors are provided by the nonlinear-regression procedure on a correlator obtained over 10 000 disorder configurations:

	D	ξ_y	ξ_t	$R_1(0)$
Grid	4	2	1	–
Gauss	10.08 ± 0.08	0.625 ± 0.005	0.312 ± 0.003	$\frac{1}{\sqrt{4\pi}}$
SincG	8.04 ± 0.02	2.020 ± 0.004	1.012 ± 0.002	$\frac{1}{\text{Erf}(\pi)}$
CubicS	7.95 ± 0.02	2.006 ± 0.004	1.005 ± 0.002	1

As we can check both in this table and visually in Fig. 10 (bottom), the sinus cardinal $\mathcal{R}^{\text{SincG}}$ catches the main phenomenological features of the exact $\mathcal{R}^{\text{CubicS}}$, i.e., the amplitude of the central peak and the position of the first oscillation, and keeps satisfied the relations $\xi_{t,y} = \xi_{t,y}^{\text{grid}}$ and $D = D^{\text{grid}}\xi_t^{\text{grid}}\xi_y^{\text{grid}}$.

As for the Gaussian fit $\mathcal{R}^{\text{Gauss}}$, it overestimates the amplitude of the peak and underestimates its typical variance. For the latter statement, it is simply due to the geometrical definitions of the parameter ξ proper to each of these functions and whose discrepancy can be merged up to a numerical constant ($\xi^{\text{CubicS}}/\xi^{\text{Gauss}} \approx 3.6$). For the first statement, it stems from the fact that a normalized Gaussian function is used to fit a normalized function which has negative contributions: The integral of the central peak has, thus, an unnormalized integral larger than 1 and fitting it by a Gaussian naturally yields a larger corresponding amplitude ($D^{\text{CubicS}}/D^{\text{Gauss}} \approx 0.80$). This discrepancy will actually be present in all the similar fitting procedures in Secs. IV and V.

APPENDIX B: SET OF PARAMETERS FOR THE NUMERICAL SIMULATIONS

We have listed thereafter the parameters of the numerical study presented throughout this paper. These parameters are defined in Sec. III.

The discretization grids for the generation of the random potential and for the recording of the data are fixed once and for all to the following values for all the computations (the last three parameters are, respectively, the number of points for the linear grid in t, the logarithmic grid in t, and the linear grid in y as defined in Fig. 3):

D^{grid}	ξ_t^{grid}	ξ_y^{grid}	nbptlint	nbptlogt	nbptliny
4	1	2	80	80	100

The following sets of data have been generated, with the elastic constant being fixed at $c = 1$ and at different temperatures T. The number of configurations "NconfV" per data set have fluctuated as a compromise between the convergence of the disorder average and a reasonable computation time, as already mentioned in Sec. III. The first column gathers the sets used for the study of $\bar{R}(t,y)$, $\widetilde{D}_t$, and $\tilde{\xi}_t$, whereas the second column corresponds to the additional sets which explore larger times $t < t_m$ and thus have been used for the study of the roughness $B(t)$:

No.	T	t_m	y_m	NconfV	t_m	y_m	NconfV
1	0.35	40	50	572			
2	0.4	40	50	1092			
3	0.5	40	50	728			
4	0.55	40	50	540			
5	0.6	40	50	654			
6	0.7	40	50	1281			
7	0.8	40	50	2665			
8	0.9	40	50	900			
9	1	40	50	1350			
10	1.1	40	50	1040	100	70	518
11	1.35	40	50	1050	300	60	390
12	1.5	40	50	1435	200	80	1600
13	1.6	40	50	1600			
14	1.8	40	50	1000	800	160	159
15	2	40	50	1750			
16	2.25	40	50	1300			
17	2.5	40	50	1900			
18	2.75	40	50	1000			
19	3	40	50	2300			
20	3.2	40	50	1000			
21	3.5	40	50	1825			
22	4	40	50	1100			
23	6	40	50	900	80	50	280

APPENDIX C: QUANTITATIVE TEST OF THE DP TOY MODEL: COMPARISON AMONG $\mathcal{R}^{\mathrm{Gauss}}$, $\mathcal{R}^{\mathrm{SincG}}$, AND $\mathcal{R}^{\mathrm{CubicS}}$

We have discussed in Secs. IV and V the time and temperature dependencies of the correlator $\bar{R}(t,y)$ from the
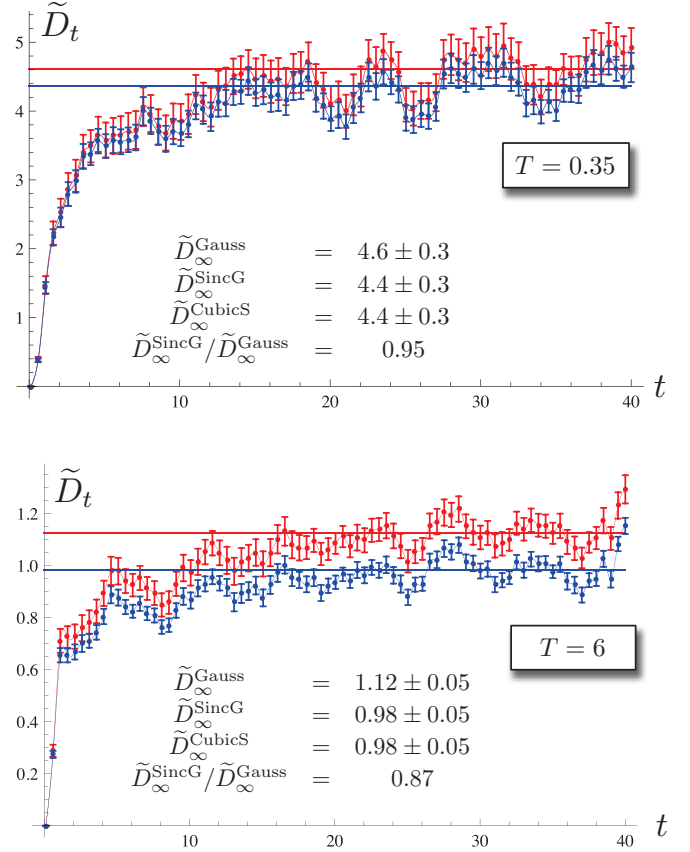

FIG. 11. (Color online) Fitting parameter $\widetilde{D}_t$ at fixed low versus high temperature $T \in \{0.35, 6\}$ with respect to Gauss (red, top) and SincG (blue, bottom), CubicS collapsing exactly on SincG. The straight lines indicate the respective average value $\widetilde{D}_\infty$ for $t > t_{\mathrm{min}} = 25$, whose standard deviation is given explicitly for each fit.

point of view of our DP toy model [(20) and (21)]. The determination of the fitting parameters $\{\widetilde{D}_t, \tilde{\xi}_t\}$, their average over large times $\{\widetilde{D}_\infty, \tilde{\xi}_\infty\}$, and the fitting parameters $\{\widehat{D}_{\mathrm{sat}}, \tilde{\xi}_{\mathrm{sat}}\}$ of the averaged correlator $\bar{R}_{\mathrm{sat}}(y)$ depends, however, on the choice of the fitting function $\mathcal{R}(y)$. We thus have gathered in this appendix the detailed quantitative comparison of the three fitting procedures with, respectively, $\mathcal{R}^{\mathrm{Gauss}}$, $\mathcal{R}^{\mathrm{SincG}}$, and $\mathcal{R}^{\mathrm{CubicS}}$.

1. Effective parameters $\{\widetilde{D}_t, \tilde{\xi}_t\}$ and their saturation values $\{\widetilde{D}_\infty, \tilde{\xi}_\infty\}$ versus $\{\widetilde{D}_{\mathrm{sat}}, \tilde{\xi}_{\mathrm{sat}}\}$

In Figs. 11 and 12, we follow the evolution of the two fitting parameters $\{\tilde{\xi}_t, \widetilde{D}_t\}$ for the same fixed low versus high temperatures $T \in \{0.35, 6\}$ as in Fig. 4, assuming that the validity of the decomposition $\bar{R}(t,y) \approx \widetilde{D}_t \mathcal{R}_{\tilde{\xi}_t}(y)$ could be extended to smaller times. Even though the DP toy model assumption *a priori* breaks down for $t < t_{\mathrm{sat}}$, the three fits yield consistent values both for $\widetilde{D}_t$ and $\tilde{\xi}_t$, with reasonable uncertainties even at short times (see the error bars in Figs. 11 and 12). On one hand, we recover for $\widetilde{D}_t$ the two regimes observed for the correlator $\bar{R}(t,y)$, i.e., an increase of this amplitude at short times and a saturation beyond t_{sat} as indicated by the straight lines $\widetilde{D}_\infty$ in Fig. 11 (obtained by
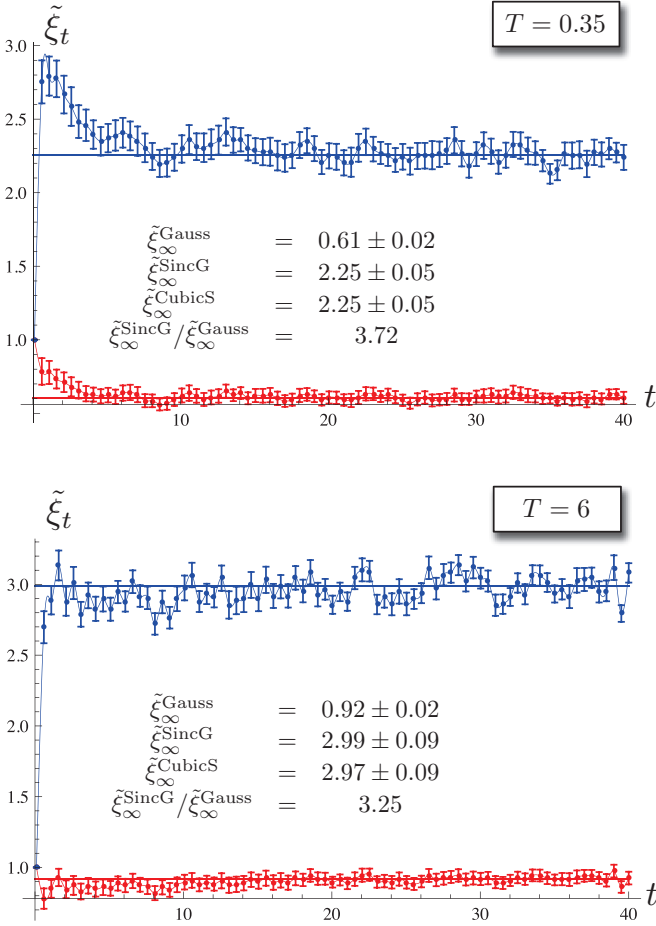
FIG. 12. (Color online) Fitting parameter $\tilde{\xi}_t$ at fixed low versus high temperature $T \in \{0.35, 6\}$, computed conjointly to $\widetilde{D}_t$ of Fig. 11 and following the same convention regarding the legend with respect to Gauss (red, bottom) and SincG (blue, top).

TABLE I. Fitting parameters $\{\tilde{\xi}_{\rm sat}, \widetilde{D}_{\rm sat}\}$ at $T \in \{0.35, 1, 6\}$, computed from the saturation correlators $\bar{R}_{\rm sat}(y)$ plotted in Fig. 4 for $t_{\rm min} = 25$. These values are almost identical to the average of the fitting parameters $\{\tilde{\xi}_\infty, \widetilde{D}_\infty\}$ over the same time range $t > t_{\rm min}$.

$(t > t_{\rm min} = 25)$	$T = 0.35$	$T = 1$	$T = 6$
$\widetilde{D}_{\rm sat}^{\rm Gauss}$	4.6 ± 0.2	4.3 ± 0.2	1.13 ± 0.04
$\widetilde{D}_{\rm sat}^{\rm SincG}$	4.4 ± 0.2	3.9 ± 0.2	0.99 ± 0.03
$\widetilde{D}_{\rm sat}^{\rm CubicS}$	4.37 ± 0.07	3.89 ± 0.05	0.98 ± 0.06
$\widetilde{D}_{\rm sat}^{\rm SincG}/\widetilde{D}_{\rm sat}^{\rm Gauss}$	0.95	0.91	0.87
$\tilde{\xi}_{\rm sat}^{\rm Gauss}$	0.61 ± 0.04	0.70 ± 0.04	0.92 ± 0.04
$\tilde{\xi}_{\rm sat}^{\rm SincG}$	2.25 ± 0.07	2.42 ± 0.05	2.99 ± 0.06
$\tilde{\xi}_{\rm sat}^{\rm CubicS}$	2.25 ± 0.07	2.40 ± 0.05	2.97 ± 0.06
$\tilde{\xi}_{\rm sat}^{\rm SincG}/\tilde{\xi}_{\rm sat}^{\rm Gauss}$	3.72	3.45	3.25

A quantitative benchmark is nevertheless available for the comparison among $\mathcal{R}^{\rm Gauss}$, $\mathcal{R}^{\rm SincG}$, and $\mathcal{R}^{\rm CubicS}$. It consists in applying our whole fitting procedure on the *linearized* correlator $\bar{R}^{\rm lin}(t, y)$ (24) corresponding to our microscopic disorder correlator $R_\xi(y) = R_\xi^{\rm CubicS}(y)$ (depicted in Fig. 2). We refer the reader to our analytical paper [42] for the exact computation of $\bar{R}^{\rm lin}(t, y)$. We thus determine the correlator $\bar{R}^{\rm lin}(t, y)$ at $\{\xi = 2, c = D = T = 1\}$, and we compute its fitting parameters $\{\widetilde{D}_t, \tilde{\xi}_t\}$ using the Gauss and the SincG fitting functions. Averaging it over a set of times $t > t_{\rm min}$, we then extract on one hand the average of its parameters $\{\widetilde{D}_\infty, \tilde{\xi}_\infty\}$ and on the other hand its averaged correlator $\bar{R}_{\rm sat}^{\rm lin}(y)$ of parameters $\{\widetilde{D}_{\rm sat}, \tilde{\xi}_{\rm sat}\}$. We obtain for $T = 1$ the following geometrical ratios: $\frac{\widetilde{D}_\infty^{\rm SincG}}{\widetilde{D}_\infty^{\rm Gauss}} = \frac{\widetilde{D}_{\rm sat}^{\rm SincG}}{\widetilde{D}_{\rm sat}^{\rm Gauss}} \approx 0.89$ and $\frac{\tilde{\xi}_\infty^{\rm SincG}}{\tilde{\xi}_\infty^{\rm Gauss}} = \frac{\tilde{\xi}_{\rm sat}^{\rm SincG}}{\tilde{\xi}_{\rm sat}^{\rm Gauss}} \approx 3.27$. These ratios are in a surprisingly good *quantitative* agreement with the high-T case given in Table I. This agreement supports the idea that at high T we recover the microscopic disorder correlator $\bar{R}(\infty, y) \approx \frac{cD}{T} \mathcal{R}_{\tilde{\xi}_\infty}^{\rm CubicS}(y)$, taking into account the artifact of the large-y asymptote in the determination of the fitting parameters. Finally, we have checked that these ratios depend only slightly on the value of the temperature, decreasing for both $\widetilde{D}$ and $\tilde{\xi}$ when T increases (the same trend as in Table I).

2. Evolution of the peak $\bar{R}(t, 0) \sim \widetilde{D}_t/\tilde{\xi}_t$

The short-times behavior of the fitting parameters $\{\widetilde{D}_t, \tilde{\xi}_t\}$ can have either a deep physical meaning or be an artifact due to the inadequacy of the fitting function $\mathcal{R}(y)$ for the measured correlator $\bar{R}(t, y)$. Note, for instance, that the short-time increase of $\widetilde{D}_t$ is compatible with the analytical predictions discussed in Ref. [42].

An additional characterization of the time evolution of the correlator's shape $\mathcal{R}(y)$ consists in comparing the evolution of the peak $\bar{R}(t, 0)$ deduced from the three fits, Gauss, SincG, and CubicS (combining $\mathcal{R}_{\tilde{\xi}=1}^{\rm fit}(0)$, $\widetilde{D}_t^{\rm fit}$, and $\tilde{\xi}_t^{\rm fit}$), to the value measured numerically. This provides a consistency check, on the whole time range available, that there is a temperature crossover in the shape of the correlator.

In Fig. 13 (top) we see that at low T the peak is correctly captured by Gauss, and, when increasing the temperature, the relative difference between the fits decreases. However,
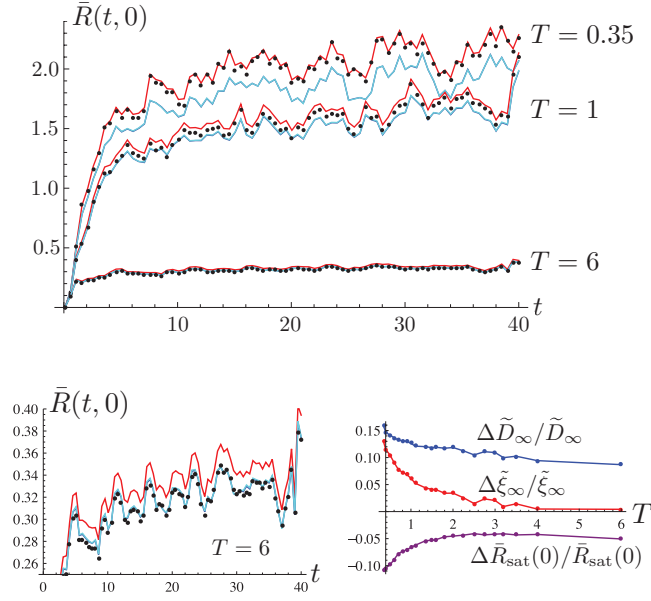
averaging $\widetilde{D}_t$ over $t > t_{\rm min} = 25$). On the other hand, $\tilde{\xi}_t$ slightly decreases at short times and its saturation seems to appear much sooner, especially at high T.

As a self-consistency check, we can notice that the average of the fitting parameters $\{\tilde{\xi}_\infty, \widetilde{D}_\infty\}$ have the same values as the fitting parameters of the averaged correlator $\{\tilde{\xi}_{\rm sat}, \widetilde{D}_{\rm sat}\}$ listed in Table I. Their estimated errors are actually surprisingly close, even though they have distinct origins, stemming respectively from the variance of $\{\tilde{\xi}_t, \widetilde{D}_t\}$ at $t > t_{\rm min}$ and from the uncertainty over the fit of $\bar{R}_{\rm sat}(y)$.

If the function $\mathcal{R}_{\tilde{\xi}_t}(y)$ did coincide exactly with the microscopic disorder correlator $R_\xi^{\rm CubicS}(y)$ at small y and large times, we would expect to have the following geometrical ratios $\frac{\widetilde{D}_\infty^{\rm SincG}}{\widetilde{D}_\infty^{\rm Gauss}} = \frac{D^{\rm SincG}}{D^{\rm Gauss}} \approx 0.80$ and $\frac{\tilde{\xi}_\infty^{\rm SincG}}{\tilde{\xi}_\infty^{\rm Gauss}} = \frac{\xi^{\rm SincG}}{\xi^{\rm Gauss}} \approx 3.6$ as discussed in Appendix A. Despite the temperature dependence of $\{\tilde{\xi}_\infty, \widetilde{D}_\infty\}$ discussed in Sec. V, these ratios are numerically found to be of the expected order of magnitude and reasonably constant for different values of $t_{\rm min}$ at fixed T (cf. Table I). However, as discussed in Sec. IV, the average procedure over $t > t_{\rm min}$ introduces an overall negative shift of the large-y asymptote of $\bar{R}_{\rm sat}(y)$ and this artifact will inevitably alter the geometrical ratios.

FIG. 14. (Color online) Temperature dependence of $\widetilde{D}_\infty$ with respect to Gauss (red, top) and SincG (blue, bottom). The straight line cD/T indicates the expected behavior in the high-T regime ($cD = 8$ for our data). Inset: Corresponding mean and standard deviation for the average of $\widetilde{D}_t$ over $t > t_{\min} = 25$.

FIG. 13. (Color online) Top: Time evolution of the maximum of the correlator peak $\bar{R}(t,0)$ at fixed temperature $T \in \{0.35,1,6\}$ measured numerically (black dots) or predicted by the fitting functions via $\bar{R}^{\mathrm{fit}}(t,0) = \mathcal{R}^{\mathrm{fit}}_{\tilde{\xi}=1}(0)\,\widetilde{D}^{\mathrm{fit}}_t/\tilde{\xi}^{\mathrm{fit}}_t$ {(top) red for Gauss (35) and blue for SincG (36); (bottom) cyan for CubicS [(A2) and (A3)]}. The curves for SincG and CubicS systematically coincide. Bottom left: Close-up of the high-T case, where the SincG and CubicS predict more accurately the peak at high T, whereas at low T Gauss seems more suited. Bottom right: Decrease in the relative differences between the Gauss and SincG parameters with increasing temperature, averaged on the large-time window $t \in [25,40]$: $\frac{\Delta\widetilde{D}_\infty}{\widetilde{D}_\infty} = \frac{\widetilde{D}^{\mathrm{SincG}}_\infty - \widetilde{D}^{\mathrm{Gauss}}_\infty}{\widetilde{D}^{\mathrm{SincG}}_\infty}$, $\frac{\Delta\tilde{\xi}_\infty}{\tilde{\xi}_\infty} = \frac{\tilde{\xi}^{\mathrm{SincG}}_\infty - \tilde{\xi}^{\mathrm{Gauss}}_\infty \xi^{\mathrm{SincG}}/\xi^{\mathrm{Gauss}}}{\tilde{\xi}^{\mathrm{SincG}}_\infty}$ (see the end of Appendix A), and $\frac{\Delta\bar{R}_{\mathrm{sat}}(0)}{\bar{R}_{\mathrm{sat}}} = \frac{\bar{R}^{\mathrm{SincG}}_{\mathrm{sat}}(0) - \bar{R}^{\mathrm{Gauss}}_{\mathrm{sat}}(0)}{\bar{R}^{\mathrm{SincG}}_{\mathrm{sat}}(0)}$.

zooming on the high T (bottom left) we see that CubicS' and SincG catch the peak more precisely. Comparing the relative differences between the fits as a function of T (bottom right), two temperature regimes can be postulated regarding the normalized function $\mathcal{R}(y)$: at high T we have $\mathcal{R}(y) \approx \mathcal{R}^{\mathrm{CubicS}}(y)$ with the relative behavior between the fits as expected from Appendix A (geometrical collapse of $\tilde{\xi}^{\mathrm{SincG}}_\infty/\tilde{\xi}^{\mathrm{Gauss}}_\infty \approx \xi^{\mathrm{SincG}}/\xi^{\mathrm{Gauss}}$, overestimation of the amplitude and, thus, of the peak by Gauss); at low T the modification of the function $\mathcal{R}(y)$ is essentially pushed into the increasing discrepancy $\Delta\tilde{\xi}_\infty/\tilde{\xi}_\infty$. Let us emphasize that the zero-temperature limit of $\bar{R}(\infty,y)$, and, hence, its normalized shape $\mathcal{R}(y)$, are not known analytically.

3. Temperature dependence of $\widetilde{D}_\infty$ and $\tilde{\xi}_\infty$

We conclude the quantitative comparison of the three fitting procedures $\mathcal{R}^{\mathrm{Gauss}}$, $\mathcal{R}^{\mathrm{SincG}}$, and $\mathcal{R}^{\mathrm{CubicS}}$ by discussing the temperature dependence of the asymptotic amplitude $\widetilde{D}_\infty$ and typical spread $\tilde{\xi}_\infty$.

The measured amplitude $\widetilde{D}_\infty$ as a function of T is reported in Fig. 14 for both Gauss and SincG (which collapses with CubicS) fits. Qualitatively, it decreases in $1/T$ at high T
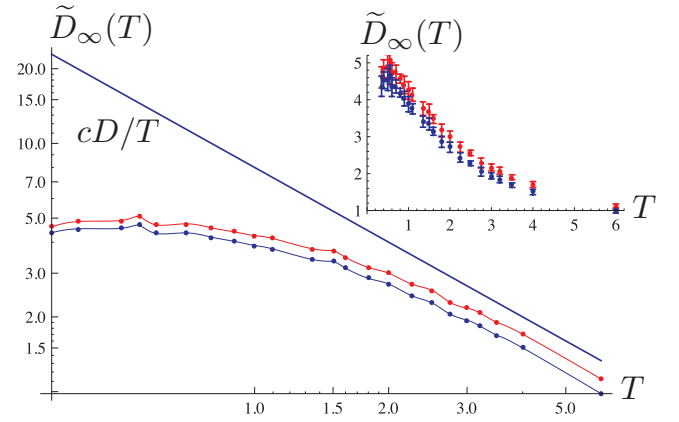
and saturates at low T, as detailed in Ref. [42], according to the scaling arguments and GVM predictions of the full model and the DP toy model. A parametrization of this temperature crossover has been defined in the relation $\widetilde{D}_\infty(T,\xi) = f(T,\xi)\frac{cD}{T}$ (19) with the interpolating parameter $f(T,\xi)$. Quantitatively, its $\xi = 0$ limit requires at high T to have $f \lesssim 1$ without any additional numerical prefactor but extracting the strength of disorder D from the $1/T$ behavior of $\widetilde{D}_\infty$ actually yields a systematic underestimation with
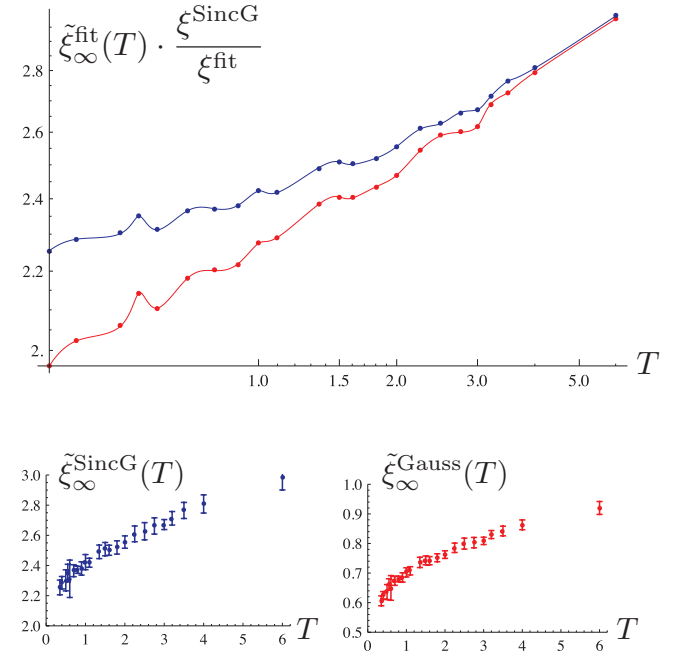

FIG. 15. (Color online) Top: Temperature dependence of $\tilde{\xi}_\infty$ with respect to Gauss (red, bottom) and SincG (blue, top), normalized for Gauss with $\xi^{\mathrm{SincG}}/\xi^{\mathrm{Gauss}} \approx 3.6$ (cf. Appendix A). Bottom: Corresponding mean and standard deviation for the average of $\tilde{\xi}_t$ over $t > t_{\min} = 25$.

respect to the microscopic disorder: $D^{\text{Gauss}} = 6.72 \pm 0.08$, $D^{\text{SincG}} = 5.92 \pm 0.05$, and $D^{\text{CubicS}} = 5.89 \pm 0.05$ (obtained on the three larger available temperatures), whereas $D = 8$ (33). As in Sec. C 1, we attribute again this discrepancy to the negative excursions of $\bar{R}(t,y)$ at large y [the contribution $b(t,y)$ in (25)] which bias all the fits and preclude a quantitative test of $f(T,\xi)$ with respect to the GVM prediction (recalled after (19) and discussed in Ref. [42]).

Finally, the typical spread $\tilde{\xi}_\infty$ obtained in parallel to $\tilde{D}_\infty$ is reported in Fig. 15. The collapse of the different fits for $\tilde{\xi}_\infty$ has already been discussed in Sec. C 1; it is compatible with the scenario of a high-T correlator, $\mathcal{R}_{\text{sat}}(y) \approx \mathcal{R}^{\text{CubicS}}(y)$. However, it displays a temperature dependence that *a priori* corrects to first order the minimal assumption that $\tilde{\xi}_\infty \approx \xi$ in our DP toy model, since the thermal fluctuations seem to increase the effective $\tilde{\xi}_\infty$ compared to the microscopic disorder correlation length $\xi^{\text{grid}} = 2$ (which consistently remains a lower bound in our measured $\tilde{\xi}_\infty^{\text{CubicS}}$). We know from the linearized solution (24) that neglecting the KPZ nonlinearity we recover asymptotically $\frac{cD}{T}\mathcal{R}_\xi^{\text{CubicS}}(y)$ for the correlator, so any modification of $\tilde{\xi}_\infty$ in this two-point correlator can only stem from the KPZ nonlinearity at high T. A numerical artifact similar to the underestimation of $\tilde{D}_\infty$ is not to be excluded, but no more conclusions can be drawn from our numerical results.

APPENDIX D: FLUCTUATIONS OF $\overline{\bar{F}_V(t,y)}$

We present in the Appendix a study of the *mean value* of the disorder free energy. Its time dependence yields an alternative measurement of the *two-point correlator maximum* $\bar{R}(t,0)$. It thus provides an independent measurement of $\bar{R}_{\text{sat}}(0) \sim \tilde{D}_\infty/\tilde{\xi}_\infty$, incorporated in Fig. 6 and discussed in Sec. V.

In its initial definition the disorder free energy $\bar{F}_V(t,y)$ is defined up to a constant $\text{cte}_V(t)$ depending of the chosen path-integral normalization of $W_V(t,y)$ in (1). As far as statistical averages with quenched disorder are concerned, such as the roughness $B(t)$, this constant is irrelevant and, thus, usually completely skipped. The Feynman-Kac equation (14) actually yields a univocal definition of $\bar{F}_V(t,y)$ which satisfies the STS (13). In our numerical approach $\overline{\bar{F}_V(t,y)} = \text{cte}(t)$ is in fact a tractable quantity which provides an independent way to measure $\bar{R}_{\text{sat}}(y=0)$ from its large-times linear evolution. This is remarkable and a direct consequence of the KPZ nonlinearity, since linearizing (14) trivially predicts $\overline{\bar{F}_V^{\text{lin}}(t,y)} = 0$, while averaging over disorder the tilted KPZ equation (14) yields, on the contrary,

$$\partial_t \overline{\bar{F}_V(t,y)} = -\frac{1}{2c}\overline{[\partial_y \bar{F}(t,y)]^2} = -\frac{1}{2c}\bar{R}(t,0). \quad \text{(D1)}$$

Therefore, the nonlinearity induces a large-time behavior of $\overline{\bar{F}_V(t,y)}$ which must be affine in t if we assume that the free-energy fluctuations saturate for times $t > t_{\text{sat}}$ as in (21). In other words, we expect at $t > t_{\text{sat}}$,

$$-2c\,\overline{\bar{F}_V(t,y)} = \int_0^{t_{\text{sat}}} dt'\,\bar{R}(t',0) + (t - t_{\text{sat}})\,\bar{R}_{\text{sat}}(0). \quad \text{(D2)}$$
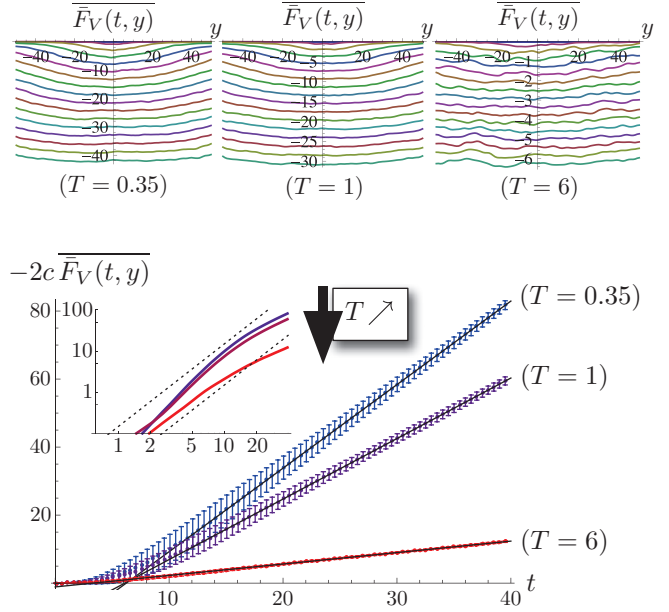

FIG. 16. (Color online) Disorder average of $\bar{F}_V(t,y)$ at fixed temperature $T \in \{0.35,1,6\}$. Top: $\overline{\bar{F}_V(t,y)}$ as a function of y for increasing times $t \in [0.1,40]$ with time steps $\Delta t = 2.5$ (top to bottom). Bottom: $-2c\,\overline{\bar{F}_V(t,y)}$ averaged over y as a function time, the error bars indicating the corresponding standard deviation; the result of the linear fit for $t > t_{\text{min}} = 25$ is indicated by the straight lines in black. Inset: Zoom on the short-time behavior in a logarithmic scale, which shows qualitatively the existence of a saturation time $t_{\text{sat}} \lesssim 10$ marking the beginning of the linear regime at large times (the dotted lines guide the eye for a quadratic behavior $\sim t^2$ as predicted analytically in Ref. [42]).

This prediction provides an additional graphical estimation of t_{sat} from the breakdown of the affine behavior of $\overline{\bar{F}_V(t,y)}$.

In Fig. 16 we have plotted the disorder average of $\bar{F}_V(t,y)$ at the same fixed temperature $T \in \{0.35,1,6\}$ as in Fig. 4, keeping, first, the spatial resolution in (t,y) (top) and then averaging over the y direction (bottom). $\overline{\bar{F}_V(t,y)}$ should be y independent, but at short time and low T it displays a slight curvature that we attribute to the artificial thermal condition at $t_0 = 0.1$. The resulting standard deviation is strongly reduced at higher T where this initial condition is more accurate with respect to thermal fluctuations.

At large times $\overline{\bar{F}_V(t,y)}$ follows a robust linear behavior which extends down to $t_{\text{sat}} \lesssim 10$, as emphasized in Fig. 16. Below t_{sat} no clear power law could be identified although the logarithmic scale in Fig. 16 makes explicit a superlinear short-time behavior, *a priori* conditioned by the initial thermal condition and not incompatible with the analytical prediction $\sim t^2$ in Ref. [42]. The temperature dependence of the averaged slope $-2c\,\partial_t \overline{\bar{F}_V(t,y)}$ yields an independent measurement of $\bar{R}_{\text{sat}}(0)$ and as such has been included in Fig. 6 in Sec. V. We find an excellent agreement between these quantities, with a slight crossover of the direct measurement from the Gauss to the SincG fits and a systematic overestimation of $-2c\,\partial_t \overline{\bar{F}_V(t,y)}$; this last point is an artifact of the short-times curvature in y of $\overline{\bar{F}_V(t,y)}$.

[1] A.-L. Barabàsi and H. E. Stanley, *Fractal Concepts in Surface Growth* (Cambridge University Press, Cambridge, UK, 1995).

[2] T. Halpin-Healy and Y.-C. Zhang, Phys. Rep. **254**, 215 (1995).

[3] J. Krug, Adv. Phys. **46**, 139 (1997).

[4] S. Lemerle, J. Ferré, C. Chappert, V. Mathet, T. Giamarchi, and P. Le Doussal, Phys. Rev. Lett. **80**, 849 (1998).

[5] V. Repain, M. Bauer, J.-P. Jamet, J. Ferré, A. Mougin, C. Chappert, and H. Bernas, Europhys. Lett. **68**, 460 (2004).

[6] P. J. Metaxas, J. P. Jamet, A. Mougin, M. Cormier, J. Ferré, V. Baltz, B. Rodmacq, B. Dieny, and R. L. Stamps, Phys. Rev. Lett. **99**, 217208 (2007).

[7] T. Tybell, P. Paruch, T. Giamarchi, and J.-M. Triscone, Phys. Rev. Lett. **89**, 097601 (2002).

[8] P. Paruch, T. Giamarchi, and J.-M. Triscone, Phys. Rev. Lett. **94**, 197601 (2005).

[9] N. A. Pertsev, D. A. Kiselev, I. K. Bdikin, M. Kosec, and A. L. Kholkin, J. Appl. Phys. **110**, 052001 (2011).

[10] K. A. Takeuchi and M. Sano, Phys. Rev. Lett. **104**, 230601 (2010).

[11] K. A. Takeuchi, M. Sano, T. Sasamoto, and H. Spohn, Sci. Rep. **1**, 34 (2011).

[12] K. A. Takeuchi and M. Sano, J. Stat. Phys. **147**, 853 (2012).

[13] J. Zhang, Y.-C. Zhang, P. Alstrøm, and M. Levinsen, Physica A **189**, 383 (1992).

[14] J. Maunuksela, M. Myllys, O.-P. Kähkönen, J. Timonen, N. Provatas, M. J. Alava, and T. Ala-Nissila, Phys. Rev. Lett. **79**, 1515 (1997).

[15] M. Alava and K. Niskanen, Rep. Prog. Phys. **69**, 669 (2006).

[16] M. Alava, M. Dube, and M. Rost, Adv. Phys. **53**, 83 (2004).

[17] S. Santucci, R. Planet, K. J. Måløy, and J. Ortín, Europhys. Lett. **94**, 46005 (2011).

[18] E. Agoritsas, V. Lecomte, and T. Giamarchi, Physica B **407**, 1725 (2012).

[19] M. Mézard, J. Phys. **51**, 1831 (1990).

[20] S. F. Edwards and D. R. Wilkinson, Proc. R. Soc. London A **381**, 17 (1982).

[21] M. Kardar, G. Parisi, and Y.-C. Zhang, Phys. Rev. Lett. **56**, 889 (1986).

[22] M. Prähofer and H. Spohn, Phys. Rev. Lett. **84**, 4882 (2000).

[23] I. Corwin, Random Matrices: Theory Appl. **01**, 1130001 (2012).

[24] K. Johansson, Commun. Math. Phys. **209**, 437 (2000).

[25] D. Forster, D. R. Nelson, and M. J. Stephen, Phys. Rev. Lett. **36**, 867 (1976).

[26] D. Forster, D. R. Nelson, and M. J. Stephen, Phys. Rev. A **16**, 732 (1977).

[27] F. Comets and N. Yoshida, J. Theor. Probab. **24**, 657 (2011).

[28] J. Krug and H. Spohn, *Solids far from Equilibrium* (Cambridge University Press, Cambridge, UK, 1991), p. 479.

[29] M. Kulkarni and A. Lamacraft, arXiv:1201.6363v1 [cond-mat.quant-gas] (2012).

[30] H. Spohn, Physica A **369**, 71 (2006).

[31] J. Rambeau and G. Schehr, Europhys. Lett. **91**, 60006 (2010).

[32] P. J. Forrester, S. N. Majumdar, and G. Schehr, Nucl. Phys. B **844**, 500 (2011).

[33] T. Kriecherbauer and J. Krug, J. Phys. A: Math. Theor. **43**, 403001 (2010).

[34] T. Sasamoto and H. Spohn, J. Stat. Mech.: Theory Exp. (2010) P11013.

[35] G. Amir, I. Corwin, and J. Quastel, Commun. Pure Appl. Math. **64**, 466 (2011).

[36] A. Borodin, I. Corwin, and P. Ferrari, arXiv:1204.1024v1 [math.PR] (2012).

[37] M. Kardar, Nucl. Phys. B **290**, 582 (1987).

[38] D. A. Huse, C. L. Henley, and D. S. Fisher, Phys. Rev. Lett. **55**, 2924 (1985).

[39] M. Balázs, J. Quastel, and T. Seppäläinen, J. Am. Math. Soc. **24**, 683 (2011).

[40] E. Agoritsas, V. Lecomte, and T. Giamarchi, Phys. Rev. B **82**, 184207 (2010).

[41] E. Agoritsas, S. Bustingorry, V. Lecomte, G. Schehr, and T. Giamarchi, Phys. Rev. E **86**, 031144 (2012).

[42] E. Agoritsas, V. Lecomte, and T. Giamarchi, Phys. Rev. E **87**, 042406 (2013).

[43] L. Bertini and N. Cancrini, J. Stat. Phys. **78**, 1377 (1995).

[44] L. Bertini and G. Giacomin, Commun. Math. Phys. **183**, 571 (1997).

[45] T. Alberts, K. Khanin, and J. Quastel, arXiv:1202.4403v1 [math.PR] (2012).

[46] R. P. Feynman, Rev. Mod. Phys. **20**, 367 (1948).

[47] M. Kac, Trans. Amer. Math. Soc. **65**, 1 (1949).

[48] M. Kardar, *Statistical Physics of Fields* (Cambridge University Press, Cambridge, UK, 2007).

[49] D. S. Fisher and D. A. Huse, Phys. Rev. B **43**, 10728 (1991).

[50] T. Hwa and D. S. Fisher, Phys. Rev. B **49**, 3136 (1994).

[51] P. Le Doussal and C. Monthus, Physica A **317**, 140 (2003).

[52] T. Sasamoto and H. Spohn, Nucl. Phys. B **834**, 523 (2010).

[53] M. Prähofer and H. Spohn, J. Stat. Phys. **108**, 1071 (2002).

[54] A. I. Larkin, Sov. Phys. JETP **31**, 784 (1970).

[55] M. Kardar, Phys. Rev. Lett. **55**, 2923 (1985).

[56] S. Bustingorry, P. Le Doussal, and A. Rosso, Phys. Rev. B **82**, 140201 (2010).

[57] A. B. Kolton, A. Rosso, and T. Giamarchi, Phys. Rev. Lett. **94**, 047002 (2005).

[58] N. J. Zabusky and M. D. Kruskal, Phys. Rev. Lett. **15**, 240 (1965).

[59] J. Quastel, in *Current Developments in Mathematics*, edited by D. Jerison, B. Mazur, T. Mrowka, W. Schmid, R. P. Stanley, and S.-T. Yau (International Press, Boston, 2012), Vol. 2011, p. 125, http://intlpress.com/site/pub/pages/journals/items/cdm/content/vols/2011/0001/00022842/index.html.

[60] D. Blömker, M. Kamrani, and S. M. Hosseini, Universität Augsburg Preprint Nr. 04/2012 (2012).

[61] MATHEMATICA tutorial for the numerical integration of differential equations: http://reference.wolfram.com/mathematica/tutorial/NDSolvePDE.html.

[62] R. Gallego, M. Castro, and J. M. López, Phys. Rev. E **76**, 051121 (2007).

[63] T. Gueudré, P. Le Doussal, A. Rosso, A. Henry, and P. Calabrese, Phys. Rev. E **86**, 041151 (2012).

[64] C.-H. Lam and F. G. Shin, Phys. Rev. E **57**, 6506 (1998).

[65] L. Balents and D. S. Fisher, Phys. Rev. B **48**, 5949 (1993).

[66] P. Chauve, T. Giamarchi, and P. Le Doussal, Phys. Rev. B **62**, 6241 (2000).

[67] T. Halpin-Healy, Phys. Rev. Lett. **109**, 170602 (2012).